Plant Physiology, 2026, 202, 1–20
https://doi.org/10.1093/plphys/kiag347
Published: 9 June 2026
Research article

Plant Physiology®

Autophosphorylation at the C-terminus of the DMI3 calmodulin-binding domain dismantles CaM-DMI3-IPD3 to initiate root nodulation

Yiting Zhou [1‡], Yuchen Qian [1*‡], Yiang Wang [1‡], Xiang Li [1‡], Yingying Huang [1], Liqiang Dai [1], Lihui Duan [1], Qian Guo [1], Kedi Jiang [1], Shang Wang [1], Jinbo Shen [2], Liqun Du [1*], and Erxu Pi [1*]

[1]College of Life and Environmental Sciences, Hangzhou Normal University, Hangzhou, China
[2]State Key Laboratory of Subtropical Silviculture, Zhejiang A & F University, Hangzhou, China

*Corresponding authors: Yuchen Qian, Email: qyc950822@163.com; Liqun Du, Email: liqundu@hznu.edu.cn; Erxu Pi, Email: erxupi@hznu.edu.cn
‡These 4 authors contributed equally to this work.
The author responsible for distribution of materials integral to the findings presented in this article in accordance with the policy described in the Instructions for Authors (https://academic.oup.com/plphys/pages/General-Instructions) is: Erxu Pi.

Abstract

The calcium/calmodulin-dependent protein kinase (CCaMK) DMI3 (Doesn't Make Infections 3) decodes rhizobia-induced Ca^{2+} signals through phosphorylation of its interacting partner, IPD3, thereby initiating root nodule symbiosis (RNS). However, the precise mechanism by which DMI3 activates this pathway remains unclear. Here, we show that phosphorylation of a triplet motif ($S^{343}S^{344}T^{345}$) located at the C-terminus of the calmodulin-binding domain acts as a molecular switch. We identified T345 as a phosphorylation site that exhibits regulatory functions similar to those of S343 and S344. Phosphomimic mutations at any single residue of the 3 sites blocked DMI3-dependent nodulation, indicating that the kinase must initially remain nonphosphorylated at these positions. Conversely, simultaneous phosphorylation of at least 2 residues was required for symbiotic activity, revealing a transition from a phosphorylation-free state to a hyperphosphorylated status (simultaneous phosphorylation of at least 2 residues) at these sites. Phosphomimic mutations within the triplet enhanced DMI3 autophosphorylation (auto-P) but severely impaired its interaction with Ca^{2+}/CaM and IPD3. In addition, the physical interaction between DMI3 and IPD3 suppressed IPD3-triggered *MtNIN* transcription and nodulation, indicating that DMI3 also acts as a negative regulator by sequestering activated IPD3. Thus, we propose a model in which repeated auto-P at the triplet contributes to RNS activation by dissociating the CaM-DMI3-IPD3 complex, thereby releasing phosphorylated and activated IPD3 to initiate the downstream transcriptional cascade. Our findings uncover a dual role for DMI3—as both a kinase and a scaffold—and clarify how auto-P within the triplet motif licenses IPD3 to trigger RNS.

Introduction

Endosymbiotic root nodule symbiosis (RNS) is a critical process that enables plants of Fabales, Fagales, Rosales, and Cucurbitales to fix up to 50 to 70 million tons of bioavailable nitrogen annually (Herridge et al. 2008). Among these, legume plants (Fabales), such as *Medicago truncatula* and *Lotus japonica*, serve as primary models for understanding the molecular mechanisms underlying RNS (Shen et al. 2020; Schulte et al. 2021; Wang et al. 2022). The legume-rhizobia symbiosis is initiated by a complex molecular dialogue that begins when root hair cells of the host plant perceive Nod factors (lipochitooligosaccharides [LCOs]) produced by rhizobia (Lerouge et al. 1990). Upon perception, these signals in turn induce cytoplasmic calcium oscillations (Ehrhardt et al. 1996; Malkov et al. 2016). The oscillatory calcium signal is decoded by *M. truncatula* DMI3 (ortholog of *L. japonicus* CCaMK) in complex with its interacting partner IPD3 (ortholog of *L. japonicus* Cyclops) (Lévy et al. 2004; Messinese et al. 2007; Yano et al. 2008; Limpens and Bisseling 2014).

Understanding how DMI3 interprets the Ca^{2+} signature has become a focal point of research since its discovery as an essential component of the RNS signaling pathway (Lévy et al. 2004; Mitra et al. 2004; Gleason et al. 2006; Tirichine et al. 2006; Hayashi et al. 2010; Wang et al. 2022). Earlier biochemical analyses in *Lilium longiflorum* have shown that LlCCaMK is activated through a 2-step mechanism: Ca^{2+} binding to its visinin-like domain with 3 EF-hands triggers T267 auto-P, thereby enhancing its affinity for Ca^{2+}/CaM. Subsequent binding of Ca^{2+}/CaM to the CBD relieves autoinhibition and stimulates substrate phosphorylation (sub-P) (Patil et al. 1995; Takezawa et al. 1996; Sathyanarayanan et al. 2001). This finding was further extended by Miller et al. (2013), who showed that Ca^{2+} binding to visinin-like

Received: October 29, 2025. **Accepted:** April 16, 2026
© The Author(s) 2026. Published by Oxford University Press on behalf of American Society of Plant Biologists. All rights reserved. For commercial re-use, please contact reprints@oup.com for reprints and translation rights for reprints. All other permissions can be obtained through our RightsLink service via the Permissions link on the article page on our site—for further information please contact journals.permissions@oup.com.

Downloaded from academic.oup.com/plphys/article/202/2/kiag347/8704448 by Hangzhou Normal University user on 03 November 2026

domain at rest condition triggers T271 auto-P (T271-P) in DMI3 (equivalent to LlCCaMK T267), fostering the formation of a hydrogen-bond network that stabilizes the intramolecular interaction and assures complete autoinhibition, thus preventing spontaneous nodulation. Accordingly, mutations at residues disrupting this H-bond network result in deregulated kinase activities and spontaneous nodulations which share an ontogeny similar to rhizobial-induced root nodules (Gleason et al. 2006; Tirichine et al. 2006). In vitro kinase assays showed that auto-P of DMI3 at T271 or equivalents could be suppressed or enhanced depending on whether the CaM is added before or after Ca^{2+} to the reaction mixture (Miller et al. 2013). Notably, regardless of the auto-P status at this site, CaM consistently enhances the sub-P activity of DMI3 (Takezawa et al. 1996; Gleason et al. 2006; Tirichine et al. 2006). These findings therefore indicate that Ca^{2+}/CaM binding can override the autoinhibition initiated by T271 phosphorylation. Together, these discoveries defined 2 roles for T271 phosphorylation of DMI3: sealing its kinase activities at rest condition to block spontaneous nodulation and enhancing its affinity for CaM to enhance its responses to symbiotic Ca^{2+} oscillations, which are vital for establishing endosymbiosis.

The complexity of the role of DMI3 in nodulation is further illustrated by mutations that affect its function. Deletions of DMI3 or kinase-dead mutants (eg, G30E) prevent nodulation, confirming the essential role of kinase activity in this process (Catoira et al. 2000; Tirichine et al. 2006; Miller et al. 2013). However, CCaMK mutants with alterations in their EF-hands within the visinin-like domain, despite exhibiting kinase activities and Ca^{2+}/CaM response patterns similar to those of wild-type CCaMK, fail to complement the RNS deficiency in the *ccamk-3* mutant (Shimoda et al. 2012). Moreover, even a point mutation at T265 (T265I) that drastically reduces kinase activity still supports the establishment of a fully functional root nodule symbiosis (Tirichine et al. 2006). These discoveries showed that the biological function of DMI3 is not directly proportional to its kinase activities (Gleason et al. 2006; Tirichine et al. 2006; Shimoda et al. 2012), challenging a simple on/off switcher model of DMI3 in symbioses and suggesting a more delicate regulatory mechanism.

Notably, phosphorylation at S337 in LjCCaMK (equivalent to S343 in MtDMI3) and S344 in MtDMI3 in the CaM-binding domain fine-tunes DMI3 activity. Phosphomimetic mutations (S343D/S344D) disrupt interaction with CaM and IPD3, inhibit kinase activity, and abolish symbiotic function (Liao et al. 2012; Routray et al. 2013). Although these mutations do not prevent binding between an isolated CBD peptide and CaM, they abolish CaM binding to full-length DMI3, likely by strengthening intramolecular interaction between the mutated CBD and the kinase domain (Jauregui et al. 2017). This steric hindrance accounts for the autoinhibition observed in the phosphomimetic mutants. Surprisingly, phosphoablative mutations (S343A/S344A), which do not impair kinase activity or protein interactions, still severely compromise symbiosis (Liao et al. 2012; Routray et al. 2013). While excluding CaM access to the mutated CBD reasonably explains the loss of activation of S343D/S344D mutants, why and how S343A/S344A mutations compromise DMI3 biological function is still a mystery.

These phosphorylation events converge on IPD3/CYCLOPS, a direct substrate of DMI3. DMI3-dependent phosphorylation of IPD3 at specific residues enables its recognition of cis-elements within the promoters of symbiosis-related genes, including *NIN* (*Nodule INception*), *RAM1* (*Reduced Arbuscular Mycorrhiza 1*), and *ERN1* (*AP2/ERF transcription factor*). In LjCyclops S50 and S154 were identified as residues phosphorylated by CCaMK (Singh et al. 2014). The phosphomimetic mutant LjCyclops-S50D-S154D (LjCyclopsDD), but not the wild-type LjCyclops, was found to bind distinct palindromic cis-elements in different symbiotic contexts: CYC-RERAM1 (TGGGCCGGCCCA, −289 bp) within the *LjRAM1* promoter during arbuscular mycorrhizal symbiosis; CYC-RE_{NIN} (TGCCATGTGGCA, −703 bp) in the *LjNIN* promoter, CYC-RE_{ERN1} (CCTCCATGTGGCAG, −934 bp) in the *ERN1* promoter and CYC-RE_{CBP1} (TAAATGCCGGCCTTTA, −1082 bp) in the *CBP1* (*Calcium-binding protein 1*) promoter during root nodule symbiosis (Singh et al. 2014; Pimprikar et al. 2016; Cerri et al. 2017; Gong et al. 2022). Notably, the CYC-RE cis-elements within the promoters of *ERN1* and *LjNIN* both harbor the conserved motif "CCATGTGGCA." In contrast, the corresponding CYC-RE cis-elements in *RAM1* and *CBP1* share a distinct conserved motif, "GCCGGCC." Despite these discrepancies in their core conserved motifs, all 4 types of CYC-RE cis-elements exhibit palindromic characteristics.

Taken together, these findings suggest that phosphorylation at the C-terminal end of the CBD exerts a negative regulatory effect on DMI3 kinase activity. Paradoxically, however, this apparent negative regulation is essential for productive symbiotic outcomes (Liao et al. 2012; Routray et al. 2013). How such inhibitory modifications ultimately facilitate DMI3 activation and downstream signaling remains an open question. Elucidating the mechanistic link between CBD phosphorylation, kinase regulation, and IPD3-dependent transcriptional activation is critical for understanding the intricate regulatory logic governing root nodule symbiosis.

Results

T345 is an autophosphorylation site and its phosphomimic mutation turns off RNS

Since the functional implications of documented auto-P sites failed to provide satisfactory clues on how DMI3 is regulated and activated to support the establishment of root nodulation (Gleason et al. 2006; Tirichine et al. 2006; Liao et al. 2012; Routray et al. 2013), we searched for additional regulatory sites in DMI3 and identified T345 as an auto-P site using LC-MS/MS (Figure S1). Further analyses showed that similar to S337 in LjCCaMK and S344 in DMI3 (Liao et al. 2012; Routray et al. 2013), the phosphomimic mutation T345D negatively affects its sub-P, its interaction with both CaM and innate substrate IPD3 and fails to support nodulation in functional complementation assays (Figures S2 and S3). Conversely, the phosphoablative mutation T345A, which did not significantly compromise kinase activities and even enhanced interactions with both CaM and IPD3, was able to complement the *dmi3* mutant, albeit with reduced efficiency (Figure S3). Notably, T345A also led to spontaneous nodulation (Figure S4 and Table S1). This spontaneous nodulation phenotype is consistent with those of other known DMI3 mutants (S343A and S344A) and is thought to arise from leaky kinase activity that bypasses the need for full symbiotic signaling (Liao et al. 2012; Miller et al. 2013; Routray et al. 2013). Our findings suggest that auto-P of T345 in DMI3 plays a role redundant to that of S343 and S344 in regulating RNS, as evidenced by the similar effects of phosphomimic mutations (T345D, S343D, and S344D) on sub-P, interactions with CaM and IPD3, and nodulation efficiency (Liao et al. 2012; Routray et al. 2013).

Phosphorylation at least 2 of these 3 residues in the triplet is essential for RNS

It is puzzling to identify 3 consecutive residues that seem to share negative regulatory roles. We generated all combinations of

Downloaded from academic.oup.com/plphys/article/202/2/kiag347/8704448 by Hangzhou Normal University user on 03 November 2026

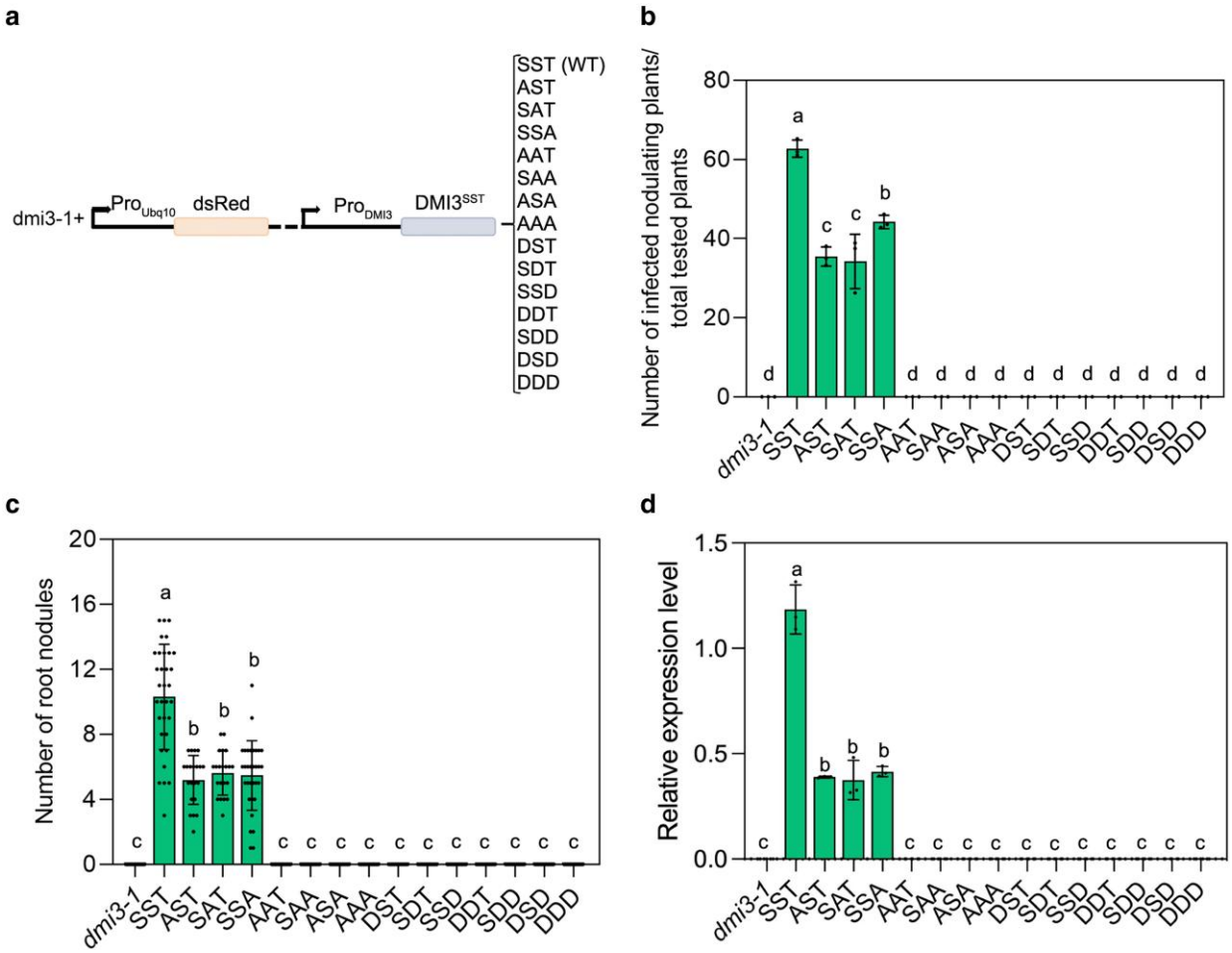


Figure 1 Two or more phosphoablative residues in the DMI3-CBD deprive root rhizobial symbiosis. Infected nodule formation was evaluated on *dmi3-1* roots transformed with *DMI3*$^{WT\ or\ mutant}$, untransformed *dmi3-1* roots were set as negative controls. (a) A schematic presentation of plasmids that carries a *Pro*$_{Ubq10}$*::dsRED* expression unit and an independent *Pro*$_{DMI3}$*::DMI3*$^{WT\ or\ mutant}$ unit. The DMI3 mutants with substitutions on residues S343, S344 and T345 were represented by a 3-character alphabet of abbreviation. For example, "DMI3^{AAA}" is short for DMI3$^{S343A,\ S344A,\ T345A}$. (b) Nodulation rate of transgenic hairy root plants after rhizobial inoculation. Each data point represents the nodulation rate, expressed as a percentage of nodulated plants relative to the total number of transformed plants (13 ~ 39 per replicate) in one biological replicate. Results are shown for 3 independent biological replicates. Different letters represent significant differences [$P < 0.05$ by one way analysis of variance with Waller-Duncan *k*-ratio *t*-test]. (c) Nodule count per plant on transgenic hairy roots with successful symbiosis. Nodule counts were quantified from nodulated plants across 3 independent biological replicates. $n \geq 47$ composite plants. Root nodules were evaluated 8 wpi. (d) Transcriptional expression of *MtNIN* gene in *dmi3-1* roots transformed with *DMI3*$^{WT\ or\ mutants}$. The relative expression level was normalized against that of the *M. truncatula ubiquitin* (*Medtr4g091580*) gene. Data are means ± SE ($n = 6$), different letters represent significant differences [$P < 0.05$ by one way analysis of variance with Waller-Duncan *k*-ratio *t*-test].

phosphoablative and phosphomimic mutants in the series of DMI3^{S343S344T345} (eg, DMI3^{S343AS344T345} [AST], SAT, SSA, AAT, SAA, ASA, and AAA) and phosphomimic (eg, DST, SDT, SSD, DDT, SDD, DSD, and DDD) mutations within the triplet. These DMI3 variants were transformed into *dmi3-1* plants, which are defective in nodulation, and their abilities to support RNS were compared to those of the wild-type DMI3^{WT} (SST) (Fig. 1a). The positive control consisted of *dmi3-1* plants transformed with *SST*, while the negative control was the untransformed *dmi3-1* mutant. Consistent with previous studies on the phosphomimic mutation at S337 in LjCCaMK or S344 in DMI3 (Liao et al. 2012; Routray et al. 2013), no root nodules were seen on the *dmi3-1* hairy roots transformed with phosphomimic single mutants. As expected, none of the phosphomimic single, double, and triple mutants supported RNS in the complementation assay (Figs. 1b, c and S5). These results confirm the constitutive presence of negative charges in the triplet resulted from phosphomimic mutation disable the ability of DMI3 function in supporting RNS. Conceivably, phosphorylation at any of the triplet residues will have a similar impact because each phosphate group carries a triple amount of negative charge. Notably, nodule formation was observed on *dmi3* hairy roots transformed with the phosphoablative single mutants AST and SAT, consistent with previous reports (Liao et al. 2012; Routray et al. 2013), as well as with the mutant SSA (this study). However, no nodules were observed on the *dmi3-1* composite hairy roots transformed with phosphoablative double and triple mutants at the end of CBD of DMI3 (Figs. 1 and S5).

To assess the molecular impact of these mutations, we analyzed the transcriptional expression of *MtNIN*, a marker gene directly regulated by the DMI3-activated IPD3 during the rhizobia infection and nodule organogenesis (Feng et al. 2021; Wang et al. 2022). The transcriptional expression of *MtNIN* was analyzed in samples collected 2 weeks post-inoculation (wpi) as described by Jin et al. (2016, 2018).

Downloaded from academic.oup.com/plphys/article/202/2/kiag347/8704448 by Hangzhou Normal University user on 03 November 2026

Consistently, RT-qPCR data revealed significantly reduced *MtNIN* expression in roots complemented with phosphoablative double and triple mutants, and all phosphomimic mutants (Fig. 1d). These results confirm the insufficient activation of the nodulation pathway in these mutants.

Apparently, a phosphoablative single mutant in which 2 residues remain phosphorylable within this triplet preserves the capability of DMI3 to initiate RNS. In contrast, when 2 or 3 residues within the triplet are prohibited from phosphorylation via mutations, the mutant no longer produced nodules in the complementation assays.This result implies that repeated phosphorylation at this triplet is essential for DMI3 to support RNS. However, the results appear to present 2 seemingly conflicting conclusions. On the one hand, repeated phosphorylation within the triplet is essential for DMI3 function in RNS. On the other hand, phosphomimetic mutations at any residue in this triplet disrupt DMI3 activity and abolish RNS support, suggesting that phosphorylation at these sites exerts an inhibitory effect. A plausible explanation for this apparent contradiction is that DMI3 activation requires a transition from an unphosphorylated state to a state in which at least 2 residues of the triplet are phosphorylated to effectively initiate RNS.

Phosphorylation at any single residue within the $S^{343}S^{344}T^{345}$ triplet enhances DMI3 auto-phosphorylation but attenuates CaM-triggered substrate phosphorylation

To elucidate interplays of auto-P at individual residues in the triplet, we examined their relevance to substrate (MtIPD3) phosphorylation (sub-P) as well as their auto-P in the presence of MtIPD3 in vitro. Consistent with previous studies (Yano et al. 2008; Liao et al. 2012; Shimoda et al. 2012; Routray et al. 2013), MtIPD3 phosphorylation by $DMI3^{WT}$ was significantly enhanced in the presence of CaM compared to its absence (Figs. 2a vs 2c, 2b vs 2d, and 2f). Notably, the kinase activities of almost all the phosphomimic mutants at S343, S344, and T345 in both auto- and sub-P were still responsive to CaM, despite most of these mutants no longer interacting with CaM except T345D (Figs. 2 and 3).

Intriguingly, a higher auto-P level was observed for any phosphomimic mutant within the triplet compared to its corresponding phosphoablative mutants in the presence or absence of Ca^{2+}/CaM (Figs. 2a, 2c, and 2e). For example, in the absence of Ca^{2+}/CaM, AST exhibited significantly lower auto-P than DST, as indicated by their superscript letters (c vs. a) (Fig. 2e). The phosphoablative triple mutant AAA exhibited the lowest auto-P; in comparison, DDD showed an apparently higher level of auto-P, even though both are unable to accept a phosphoryl group at the triplet positions (Fig. 2e). Intermediate situations were observed for double substitution mutants (Fig. 2e). Collectively, for any given number of phosphorylatable residues within the triplet, a phosphomimetic mutant consistently displayed a higher auto-P level than its phosphoablative counterpart.

In the presence of Ca^{2+}/CaM, however, the effect of phosphomimetic mutations on auto-P activity varied depending on the number of phosphorylatable residues retained. Notably, not all phosphomimetic mutants showed elevated auto-P levels relative to the SST control (Figs. 2c, and 2e). Specifically, the auto-P levels of SDD, DSD, and DDD were comparable to that of SST, whereas DDT exhibited a significantly lower auto-P level. In contrast, phosphomimetic mutants retaining 2 phosphorylatable residues—such as DST, SDT, or SSD—all displayed auto-P levels significantly higher than that of SST. Given that Ca^{2+}/CaM is generally abundant in plants under normal physiological conditions, these findings suggest that phosphorylation at any single residue within the triplet region is sufficient to enhance DMI3 auto-P. This phosphorylation may occur through a mechanism in which initial modification at 1 residue primes the enzyme for subsequent auto-p events. In other words, DMI3 auto-P within the triplet region may operate in a feed-forward manner, wherein an early phosphorylation event facilitates further phosphorylation of the protein itself.

In contrast to auto-P patterns, sub-P, which was elevated by most DMI3 mutants (except DDT), was elevated by CaM during these assays. Wild-type DMI3 (SST) exhibited almost the lowest basal sub-P activity but showed the highest increment upon CaM addition (Fig. 2f). Phosphomimic single mutants exhibited diminished increments in sub-P triggered by the addition of CaM. Compared to phosphomimic single mutants, double mutants showed even greater reductions in CaM-stimulated sub-P increments. The sub-P of the phosphomimic triple mutant DDD almost lost its response to the addition of CaM, maintaining a level similar to that of DMI3 in the absence of CaM. Meanwhile, although the phosphoablative mutants showed a decreased increment in sub-P triggered by CaM, the decrease was generally less than that observed in the phosphomimic mutants, and the phosphoablative triple mutant AAA retained its response to CaM stimulation. These results indicate that phosphorylation within the triplet generally downregulates the increment of the CaM stimulated sub-P. A plausible explanation is that the decreased affinities of phosphomimic mutants to CaM dampen their activation by CaM. Intriguingly, the phosphomimic DMI3 mutants, except for T345D, retained the capability to phosphorylate IPD3 despite losing their interacting with IPD3 (Figs. 2 and 3).

S343, S344 and T345 phosphomimic mutation disrupt the "CaM-DMI3-MtIPD3' complex.

To search for cues to address how phosphorylation in this triplet at the C-terminus of CBD of DMI3 activates RNS, we examined the effects of single, double, and triple phosphoablative and phosphomimic mutations in the triplet on the CaM binding property of DMI3. Consistent with previous studies (Liao et al. 2012; Routray et al. 2013), the CaM binding signals of the AST, SAT, SSA, AAT, SAA, ASA, and AAA were all elevated compared to that of SST, and increased by 91.27%, 31.52%, 58.57%, 29.88%, 36.18%, 39.33%, and 38.82%, respectively (Figs. 3a∼c). On the other hand, the CaM binding of DST or SDT was almost eliminated, while SSD mutation at the very end of the CBD remained at about 42.36% of CaM-binding compared with that of SST.

We further examined the interactions of the abovementioned DMI3 mutants with its native substrate MtIPD3 via a yeast-2-hybrid assay in the absence or presence of CaM, and the interaction affinities were quantitatively reflected by the β-galactosidase activities resulted from the interaction of the 2 partners. Consistent with the observations of Liao et al. (2012), the affinity of DST to IPD3 was almost unaffected; the affinities of all other phosphomimic mutants, especially those of phosphomimic double or triple mutants, were drastically decreased independent of the presence of CaM (Figure S6). To validate the above findings, we conducted a pull-down assay to further examine the interaction between DMI3 and its mutants with IPD3 under in vitro conditions. The results showed that phosphomimic mutants were unable to bind to IPD3, while the binding of phospho-ablative mutants to IPD3 was stronger than that of wild-type DMI3 (Fig. 3d). Specifically, we selected the phospho-ablative mutants with the

Downloaded from academic.oup.com/plphys/article/202/2/kiag347/8704448 by Hangzhou Normal University user on 03 November 2026

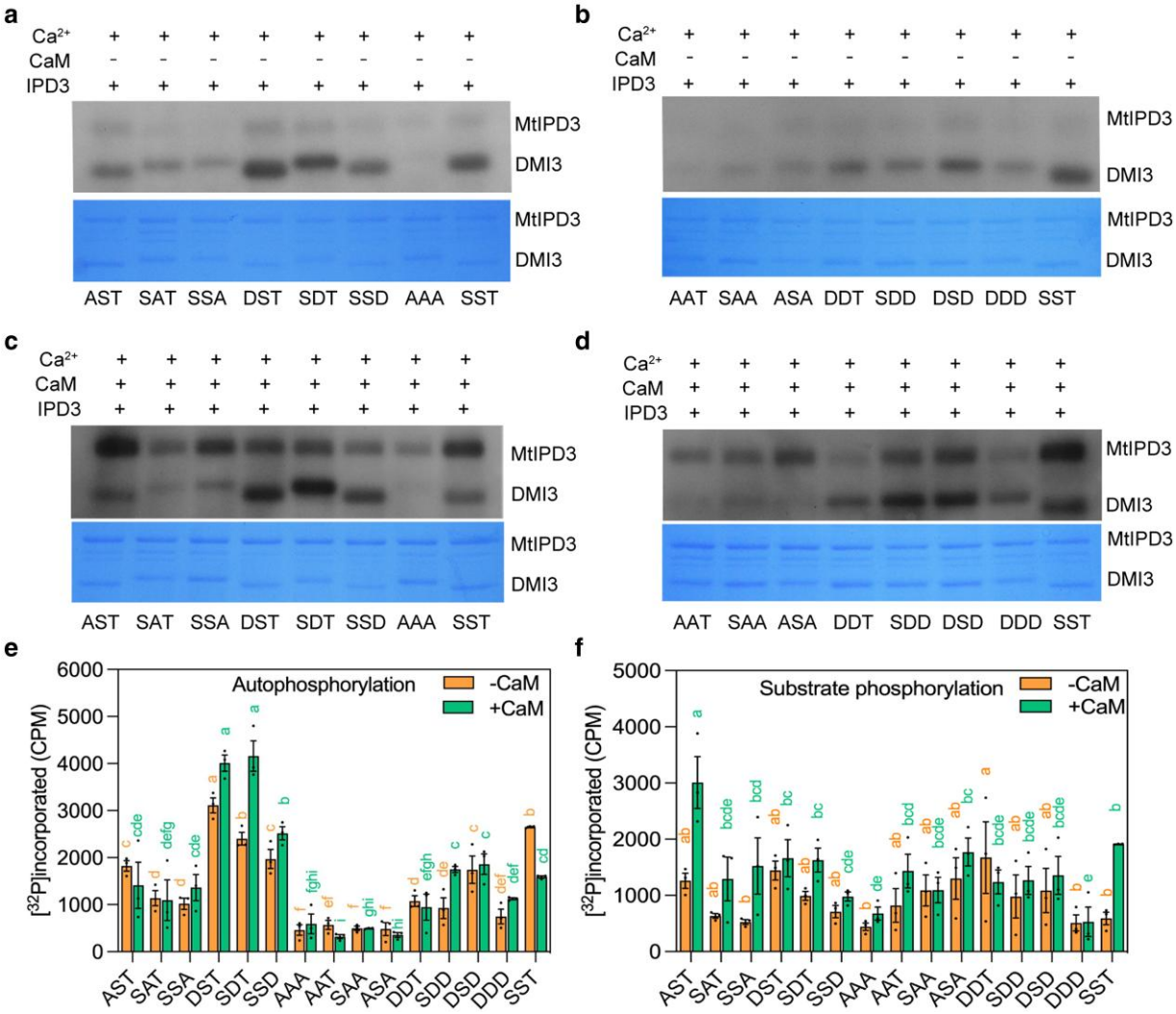


Figure 2 Impact of phosphomimic and phosphoablative mutations on kinase activities of DMI3. His-tagged DMI3 and mutants were tested for in vitro kinase activity in the presence of 0.5 mM $CaCl_2$, or 0.5 mM $CaCl_2$ and 1.0 μg CaM. Each reaction contained 0.4 μg of DMI3s-His and 0.4 μg of TrxA-MtIPD3-His. (a) and (b) Kinase assays performed without CaM. An autoradiogram is shown upper panel and a Coomassie blue staining is shown lower panel for each test. (c) and (d) Kinase assay in the presence of Ca^{2+} and CaM. An autoradiogram is shown upper panel and a Coomassie blue staining is shown lower panel for each test. (e) Quantification of auto-P in (a)-(d). Incorporation of radioactive phosphate was quantified using a liquid scintillation counter. (f) Quantification of substrate MtIPD3 phosphorylation in (a)-(d). All data are means ± SE ($n = 3$) in (e) and (f). Different letters signify statistically significant differences ($P < 0.05$), as determined by one-way analysis of variance coupled with the Waller-Duncan k-ratio *t*-test. The yellow denotes the condition absent of CaM (-CaM), whereas green signifies the presence of CaM (+CaM) in the assay.

strongest binding to IPD3 in yeast, including SST, SSA, ASA, and AAA, as representative candidates to study the effect of CaM on the DMI3-IPD3 interaction. These results confirmed that CaM weakens the interaction between DMI3 and IPD3 (Figure S7). On the other hand, none of these phosphoablative mutations in DMI3 substantially blocks its interaction with IPD3. Even the AAT mutation, which had the lowest affinity, still maintained over 70% of the binding seen with wild-type DMI3. Some phosphoablative mutations even showed increased affinity to IPD3 (Figure S6). While CaM appears to partially reduce DMI3-IPD3 interaction, complete disruption was not observed (Figure S7). Together, these results showed that phosphomimic mutations in the triplet block significantly interfere with the interaction between DMI3 and CaM, as well as that between DMI3 and IPD3, this dissociating impact is almost guaranteed when more than 1 of these 3 residues is replaced by a phosphomimic residue.

DMI3 Mutants with enhanced MtIPD3^{DD} binding suppress transactivation of *MtNIN*

As a target of the DMI3-IPD3 transcriptional complex, *MtNIN* is under elaborate regulatory control, as evidenced by its extensive promoter region of over 20 kb (Liu et al. 2019). Interestingly, the full 20-kb sequence is not required; a 1 + 5–kb fusion promoter derived from this region is sufficient to rescue symbiotic defects. This study further revealed a conserved CYC-RE motif in *NIN* orthologs across 8 legumes, though its position relative to the start codon varied widely. Follow-up work in *M. truncatula* pinpointed the functional significance of this motif, showing that the specific CYC-RE element at the −3 kb position in the *MtNIN* promoter is essential for correct infection thread formation in rhizobial symbiosis. Notably, when the *nin-1* mutant was complemented with the *NIN* coding sequence driven by a

Downloaded from academic.oup.com/plphys/article/202/2/kiag347/8704448 by Hangzhou Normal University user on 03 November 2026

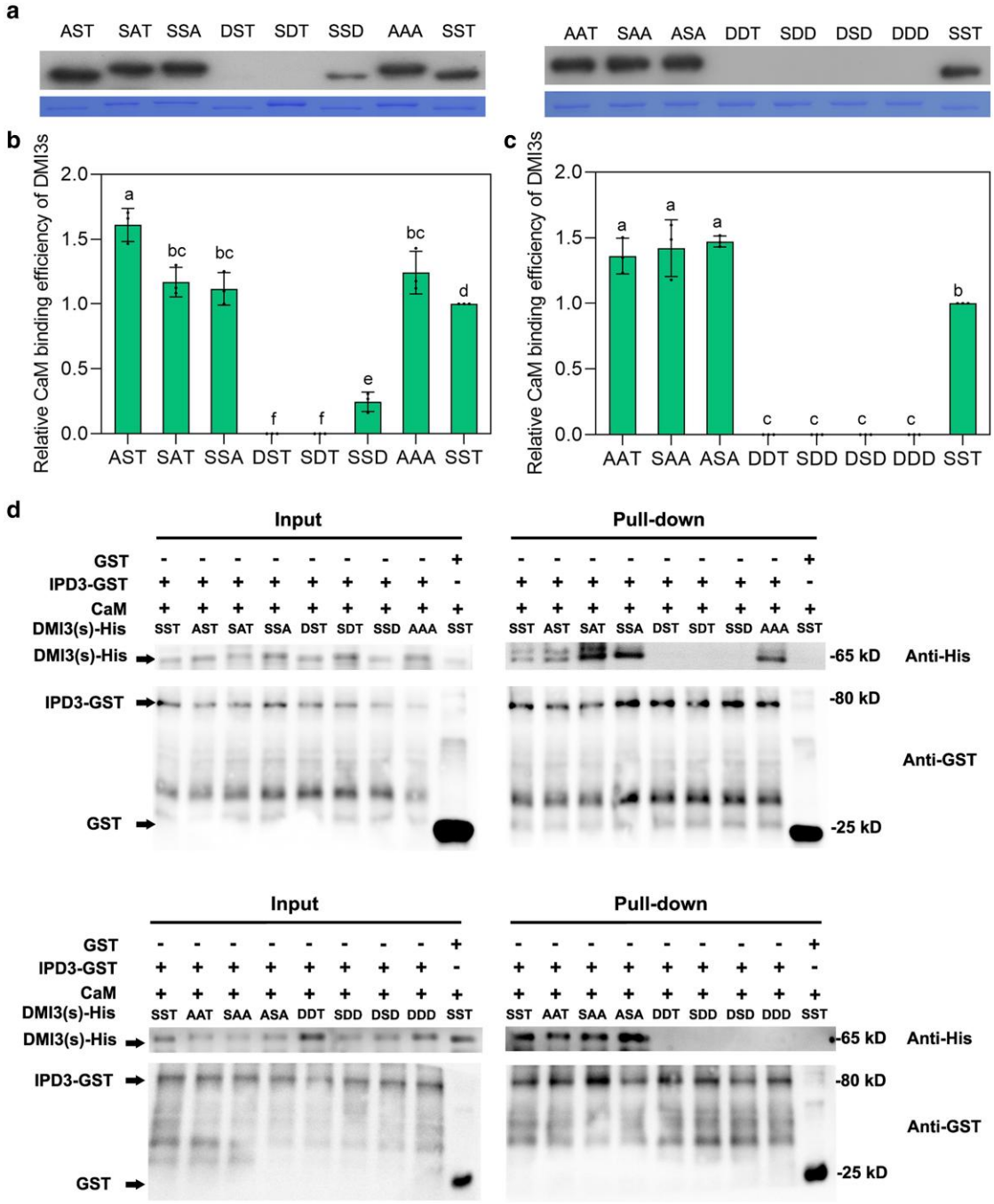


Figure 3 Impact of phosphomimic and phosphoablative mutations on DMI3 interactions with CaM and/or IPD3. (a) The effect of S343, S344 and T345 auto-P on their CaM-binding affinity was tested by transferring equal amounts (2 μg) of DMI3 and mutant proteins onto a PVDF membrane, and incubating them with CaM-HRP in the presence of 1 mM Ca^{2+}. For each test, an autoradiogram (upper panel) and Coomassie blue staining (lower panel) are shown. (b) and (c) Quantitative analysis of DMI3 and mutant proteins. The upper bands in panel (a) represent the binding of CaM-HRP to DMI3 and its mutants. To normalize binding efficiency, the intensity of the CaM-HRP bands is divided by the intensity of the Coomassie Brilliant Blue-stained DMI3/mutant bands, correcting for any loading discrepancies. The data represent the means ± SE of 3 independent replicates. (d) Pull-down assay to detect the interaction between MtIPD3 and DMI3 or its mutants. The experiments were repeated 3 times. A representative photograph is shown here. All data in (b) and (c) were statistically analyzed using the ANOVA corrected with Waller-Duncan *k*-ratio *t*-test was used to determine statistical significance. Different letters represent significant differences ($P < 0.05$).

2.2 kb proximal promoter lacking the CYC-RE, with an approximately 3% infection thread formation still formed (Liu et al. 2019), suggesting the involvement of an additional regulatory element. Supporting this hypothesis, Akamatsu et al. (2022) employed CRISPR/Cas9 to delete the CYC-RE from the *NIN* promoter in *L. japonicus*. These authors observed an approximately 40% reduction in infection thread formation in the mutant lines compared to the wild type, yet no significant differences were detected in nodule number, size, or morphology.

Downloaded from academic.oup.com/plphys/article/202/2/kiag347/8704448 by Hangzhou Normal University user on 03 November 2026

Collectively, these findings indicate that although the CYC-RE plays a critical role during early infection events, it is not the only cis-acting element to which IPD3 binds to regulate RNS (Akamatsu et al. 2022).

Although the established IPD3 binding site is well-characterized, the possibility of alternative binding venues within the extensive ~2 kb *MtNIN* promoter could not be ruled out. To address this, we implemented a targeted screening strategy, using long DNA probes (up to 500 bp) to scan the promoter for any previously uncharacterized IPD3 interaction motifs. The probes were generated by PCR with an anchored primer labeled with biotin at the 5′-end and unlabeled progressive primers matched to different locations of the templates at the 3′-end as described in the method section. Our results showed that MtIPD3^{DD} (MtIPD3$^{50D,\ 155D}$) caused an electrophoresis mobility shift of probe covering the region of −2035 to −1503 (prob-α, clear), −1539 to −983 (prob-β, weak) or −1005 to −452 (prob-γ, faint), indicating potential protein-DNA interactions (Figs. 4a~d and S8). Further analyses and fine mapping narrowed down the recognition motif to a stretch from −1931 to −1901bp. The sequence *TTTTGAAAACTTT* (designated as *IPD3-RE$_{NIN}$*), was deemed to be the target motif recognized by IPD3. To validate the recognition motif located at the very end of the EMSA probe, a 45 bp DNA from −1945 to −1901 bp carrying *IPD3-RE$_{NIN}$* (α2-1-1) was used for a site-mutation based verification test. Our results showed that unlabeled probe contained a wild-type *IPD3-RE$_{NIN}$* motif that competed with a biotin labeled probe for binding IPD3^{DD}, while a mutated probe with *IPD3-RE$_{NIN}$* mutated to *GGGGGGGGGGGGG* (α2-1-1m1) could not compete (Fig. 4d), demonstrating the sequence-specific nature of this interaction.

Previous studies have shown that Cyclops binds to palindromic CYC-box motifs, such as the TGCCATGTGGCA element in *LjNIN* (Singh et al. 2014), via symmetric homodimerization (Singh et al. 2014). Surprisingly, we identified a nonpalindromic *IPD3-RE$_{NIN}$* (TTTTGAAAACTTT) in the MtNIN promoter that displayed significantly stronger binding affinity to IPD3^{DD} than the canonical CYC-box, as demonstrated by both EMSA (Figure S9a) and microscale thermophoresis (Figure S9b). This finding challenges the prevailing model that IPD3 strictly requires palindromic sequences for dimeric binding (Singh et al. 2014), suggesting alternative modes of DNA recognition.

To determine whether this *IPD3-RE$_{NIN}$* is involved in IPD3-mediated activation of *MtNIN* (in Note S1, Jin et al. 2016), we conducted transcription analysis in *Nicotiana benthamiana* leaves using a GUS reporter under the control of either the 2035-bp *MtNIN* proximal promoter. Each promoter-reporter construct (including *mP$_{MtNIN}$::GUS* and *P$_{MtNIN}$::GUS*) was coinfiltrated with a *35S::MtIPD3^{DD}* effector construct (Figs. 4e, f, and S10). Leaves transformed with the promoter-reporter constructs alone served as negative controls. The results demonstrated that GUS activity driven by *mP$_{MtNIN}$::GUS* was significantly lower than that of *P$_{MtNIN}$::GUS*, suggesting that IPD3^{DD} can activate *MtNIN* expression through the *IPD3-RE$_{NIN}$* cis-element. Although a *CYC-RE* exists at the −3 kb location in the *MtNIN* promoter, which was reported to interact with IPD3 (Singh et al. 2014; Liu et al. 2019; Cathebras et al. 2022).

To compare the binding modes of IPD3 with the nonpalindromic *IPD3-RE$_{NIN}$* and the canonical palindromic CYC-RE motif, we performed molecular docking using AlphaFold. Structural modeling revealed that the interaction between IPD3 and DNA1 (containing the nonpalindromic *IPD3-RE$_{NIN}$* motif) is primarily stabilized by hydrogen bonds formed between basic amino acid residues and DNA bases (Figure S11a). Specifically, Arg-423 establishes a hydrogen bond with DG-21, while Arg-427 mediates sequence-specific recognition through hydrogen bonding with DT-20. The guanidinium groups of these arginine residues provide both positive electrostatic potential and strong hydrogen-bond donating capacity, facilitating directional interactions with acceptor atoms on the DNA bases and contributing to sequence- and structure-specific recognition.

In contrast, the IPD3-DNA2 complex (containing the palindromic CYC-RE motif) is stabilized by a single hydrogen bond between Ser-464 and DG-8 (Figure S11b). The hydroxyl group of Ser-464 acts as both a hydrogen bond donor and acceptor, engaging with polar atoms on the DNA base to provide a localized binding anchor. While this interaction contributes to complex stability, it imposes less stringent spatial constraints compared to the multipoint interactions observed in the IPD3-DNA1 complex.

While these in silico predictions provide valuable mechanistic insights, they represent computational models that cannot fully recapitulate the complexity of physiological DNA-protein interactions. Nevertheless, the strong concordance between the computational and experimental results reinforces the robustness of our conclusions regarding the differential recognition of these 2 cis-regulatory elements by IPD3.

Following the elucidation of the interplay between IPD3 and the *IPD3-RE$_{NIN}$* in the −2 kb promoter region of *MtNIN*, we analyzed how phosphomimic or phosphoablative mutations in this triplet in DMI3 affect the transcriptional activation of *MtNIN* driven by MtIPD3. The 2035bp *MtNIN* promoter, fused to the *uidA* gene (*P$_{MtNIN}$::GUS*), was inserted into the same construct as MtIPD3^{DD} under the control of the *35S* promoter. This construct was coexpressed in *N. benthamiana* leaf cells, with or without *DMI3* (driven by the *35S* promoter) or its mutated versions. *MtIPD3^{DD}* is an activated version of IPD3 that retains its interaction with DMI3 similarly to the situation first reported for LjCyclops (Singh et al. 2014). The activated *MtIPD3^{DD}* alone (EV + IPD3^{DD} + *pNIN::GUS*) induced strong expression of *P$_{MtNIN}$::GUS*, while coexpression with *DMI3^{WT}* (SST + IPD3^{DD} + *pNIN::GUS*) or phosphoablative mutants (DMI3 variants + IPD3^{DD} + *pNIN::GUS*) caused a significant reduction in GUS expression (Figs. 4h). On the other hand, coexpression of *DMI3* phosphomimic mutants, except DST, did not inhibit the expressions of *P$_{MtNIN}$::GUS* (Figs. 4g, h, and S12). These results suggested that the presence of DMI3 or its mutants correlates with suppressed transactivation of *MtNIN* by IPD3^{DD} in tobacco cells.

Enhanced IPD3 binding affinity of DMI3 mutants correlates with increased suppression on RNS

As a target of the DMI3-IPD3 transcriptional complexes, *NIN* functions as a key regulatory node essential for activating RNS (Schauser et al. 1999; Marsh et al. 2007; Jin et al. 2016). To explore the underlying regulatory mechanisms, we employed the constitutively active form MtIPD3^{DD} (Jin et al. 2018) as a functional mimic of the transcriptionally active version of MtIPD3. Our experimental results demonstrate that the DMI3-MtIPD3 interaction negatively regulates MtIPD3^{DD}-mediated transcriptional activation of *MtNIN* (Fig. 4h). This finding suggests that the DMI3-MtIPD3 interaction may similarly hinder RNS establishment by inhibiting *NIN* expression. A competition strategy was used to validate this hypothesis. The rational is that an extra-introduced DMI3 or its mutated version expressed from a plant expression construct in the root cells will compete for innate interaction partner MtIPD3 with the endogenous DMI3 and alter the nodulation behavior of the transgenic hairy root. Hence,

Downloaded from academic.oup.com/plphys/article/202/2/kiag347/8704448 by Hangzhou Normal University user on 03 November 2026

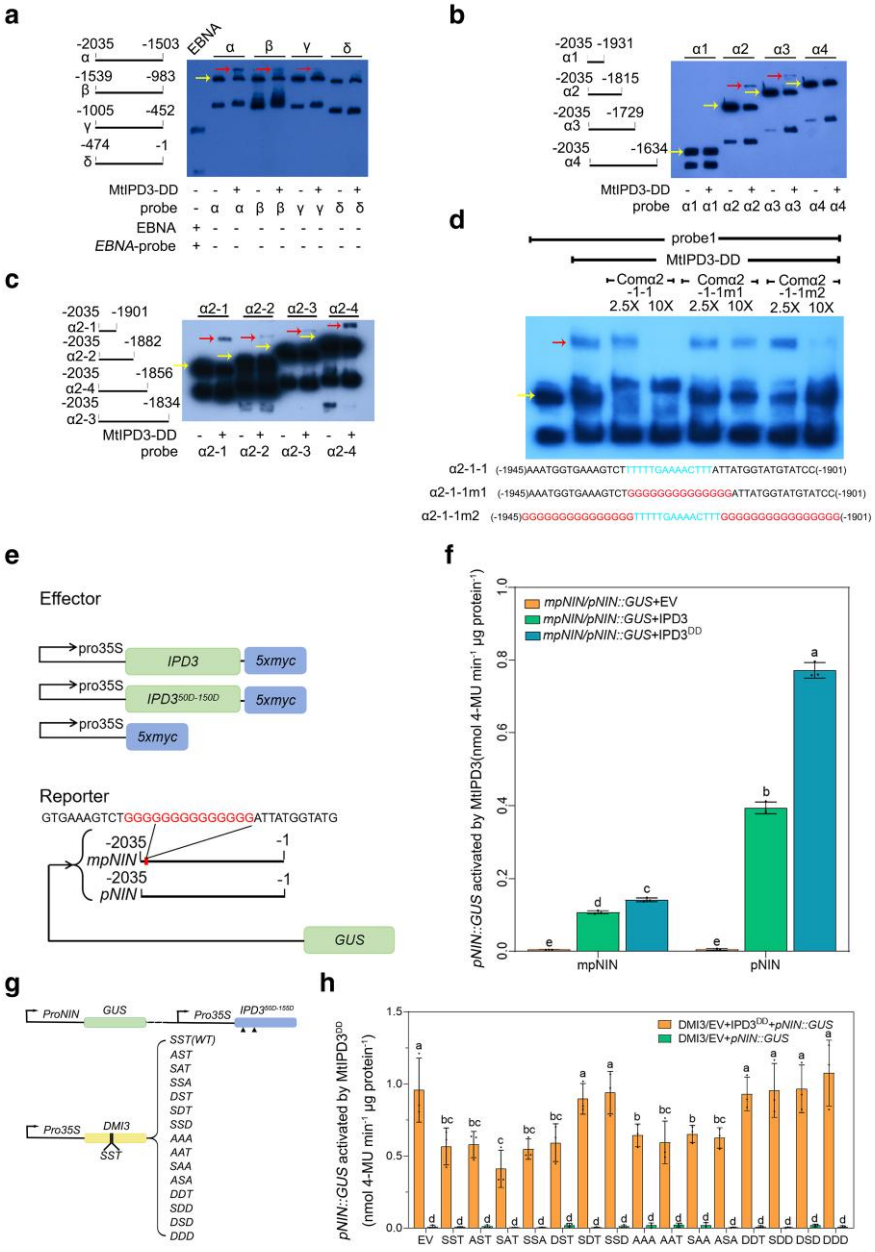


Figure 4 MtIPD3^{DD} (MtIPD3^{50D155D}) transactivates the *MtNIN* promoter is affected by DMI3-IPD3 interaction. (a)-(d) (Related to Figure S8), Identification of a unique MtIPD3^{DD} responsive cis-element in the *MtNIN* promoter using EMSA (primers in Table S7). Samples were resolved on a 6% polyacrylamide gel. The *MtNIN* promoter was selected between −2,035bp and −1 bp (Jin et al. 2016). The red arrows indicate the specific MtIPD3^{DD}-DNA complexes, and the yellow arrows mark the free, unbound probe. (a) Rough mapping identified at least 3 MtIPD3^{DD} response elements in the intervals from −2,035 to −1,503 bp (biotin-labeled α), from −1,539 to −983 bp (biotin-labeled β) and from −1,005 to −452 bp (biotin-labeled γ). (b) Fine mapping identified a MtIPD3^{DD} response element α2 (−1,931 to −1,815bp). The position of specifically bound and free probe is indicated by a red arrow and a yellow arrowhead, respectively. EBNA: Epstein-Barr Virus Nuclear Antigen, positive control. (c) Fine mapping of the α2 fragment identified a unique MtIPD3^{DD} response element (*IPD3-RE$_{NIN}$*) in −1,931 to −1,901bp (α2-1). (d) MtIPD3 specifically binds the cis-element (*TTTTGAAAACTTT*) of *MtNIN* promoter. Mutation of the palindrome (fragment M1). EMSA used 100 pmol MtIPD3^{DD} and 100 fmol biotin-labeled *IPD3-RE$_{NIN}$*. Competitor DNA carrying either the wild type or mutated *IPD3-RE$_{NIN}$* was added in 5-, 10-, or 20-fold molar excess. (e) and (f) Transactivation assays in *N. benthamiana* leaves demonstrate that the *IPD3-RE$_{NIN}$* cis-element is essential for IPD3-mediated activation of the *MtNIN* gene. (e) Schematic of cotransformed plasmids: *p35S::MtIPD3* and *pMtNIN::GUS*. (f) Quantitative GUS activity measured through β-galactosidase assays across 3 biological replicates. (g) and (h) Transactivation assay in *N. benthamiana* leaves showing that *MtIPD3^{DD}* coexpressed with *DMI3 s* lead to transcriptional activation of the *MtNIN* promoter. (g) Schematic depictions of 2 cotransformed plasmids. Specifically, one plasmid carries the *p35S::MtIPD3* expression unit and the *pMtNIN::GUS* reporter; the other carries a *p35S::DMI3* unit. (h) Quantitative analysis of GUS activity determined by β-galactosidase assays. The results shown in Fig. 4h used the vectors depicted in Fig. 4e (which contains both *pNIN::GUS* and *p35S::IPD3^{DD}*) as the reporter construct, and *p35S::DMI3* as the effector construct. The effector construct was compared to an empty vector (EV), which lacks the *DMI3* or its mutant encoding sequence (EV in Fig. 4h). The core comparison for our conclusion is between the MtIPD3DD alone (EV + IPD3^{DD} + pNIN::GUS) group and the DMI3 variants (DMI3 variants + IPD3^{DD} + pNIN::GUS) groups, and the green columns are only used to verify that DMI3 alone exerts no effect on the activity of the NIN promoter.. All the results were normalized based on the GUS enzyme activity values obtained with the EV as the effector construct. $n = 3$ biological replicates and each biological replicate was performed with five technical replicates. Different letters indicate significant differences [$P < 0.05$ by ANOVA with Waller-Duncan *k*-ratio *t*-test].

Downloaded from academic.oup.com/plphys/article/202/2/kiag347/8704448 by Hangzhou Normal University user on 03 November 2026

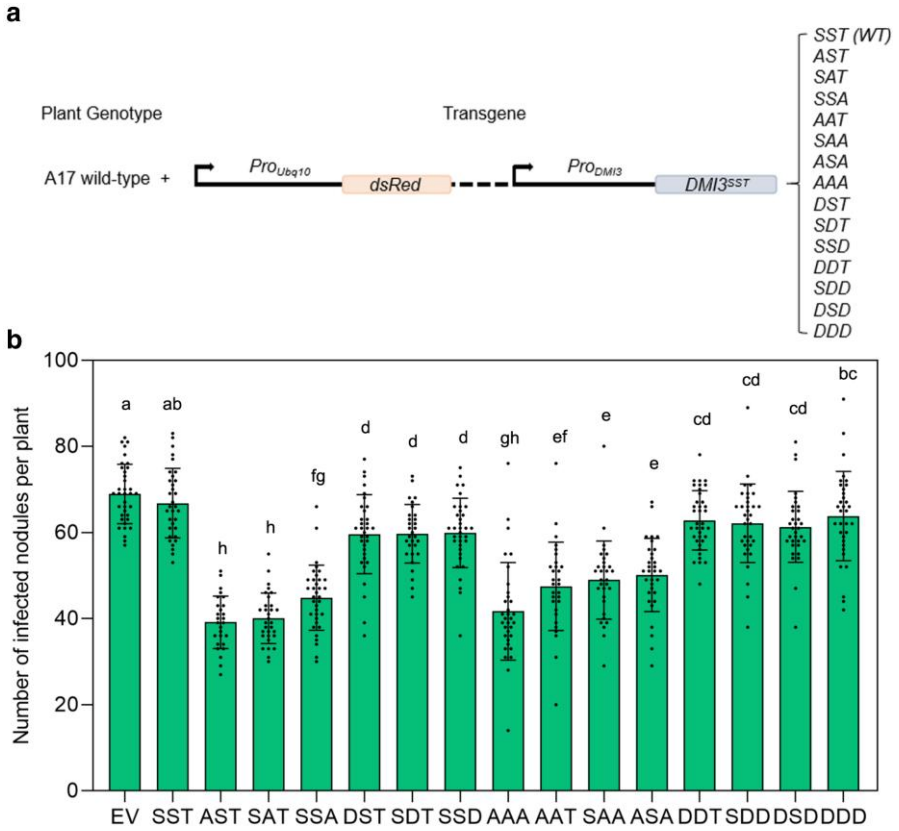


Figure 5 Effects of DMI3 and its variants on RNS in wild type hairy roots during competition assays. Infected nodule formation was evaluated on transgenic roots or untransformed wild-type accession A17 roots 8 wpi. (a) A schematic structural depiction of plasmids for hairy root transformation of *M. truncatula* A17-WT. (b) Quantitative analysis of nodule numbers on hairy roots transformed with *DMI3* or mutants. $n \geq 27$ composite plants. Number of transformed plants with nodules versus total number of transformed plants is shown for each column [All data are means ± SE. For all variables with the same letter, the difference between the means is not statistically significant. Different letters indicate statistically significant differences at $P < 0.05$ by one way analysis of variance with Waller-Duncan *k*-ratio *t*-test].

we expressed wild type *DMI3* along with its phosphomimetic and phosphoablative mutants in the hairy roots of *M. truncatula* wild type accession A17. To this end, nodule formation was evaluated on both transgenic and untransformed wild type A17 roots at 8 weeks post-inoculation with Rm1021. Nodules were observed on composite roots transformed with wild-type *DMI3* and all tested mutants (Fig. 5). A schematic structural depiction of plasmids for hairy root transformation of *M. truncatula* A17-WT (Fig. 5a). The composite roots expressing *SST* showed a similar level of nodulation efficiency as composite roots transformed with an empty vector. Although $DMI3^{SST}$ interacts with MtIPD3, it behaves exactly like the endogenous DMI3 and could be normally phosphorylated in vivo and separate from MtIPD3. Composite roots expressing phosphoablative mutants of *DMI3*, which maintain high level of interaction with MtIPD3 and are less likely or unable to be phosphorylated and separate from IPD3, produced significantly fewer root nodules (Fig. 5b). Composite roots expressing phosphomimic mutants of *DMI3*, which mostly no longer interacted with MtIPD3, showed similar or subtle decreases in nodulation efficiency compared with those expressing wild-type DMI3. It is noteworthy that DST, the only phosphomimic mutant, retained its interaction with MtIPD3 but with decreased affinity and behaved like other phosphomimic mutants in this competition assay. A possible explanation is that this mutation may have facilitated the sub-P in the triplet by facilitating its separation from MtIPD3. Together, these results support a model in which the interaction between MtIPD3 and phosphoablative DMI3 mutants in the symbiotic signaling cascade may compromise RNS establishment, suggesting that the dissociation of activated IPD3 from DMI3 facilitates nodulation.

DMI3s from Fabaceae, Cucurbitaceae, Rosaceae, and Fagaceae all have 3 residues able to accept phosphorate group

Results in the current study suggest that phosphorylation of at least 2 residues of $S^{343}S^{344}T^{345}$ in DMI3 is required for the establishment of RNS. DMI3 homologs from nonleguminous plants were reported to complement *dmi3-1* null mutants to varying degrees. LlCCaMK from *L. longiflorum*, which has 2 residues able to take phosphorate groups at the sites equivalent to $S^{343}S^{344}T^{345}$ in DMI3, was shown to restore full functional nodulation to *dmi3-1* although not as efficiently as DMI3 (Gleason et al. 2006). In contrast, rice OsCCaMK possesses only 1 such residue (within the region $S^{335}C^{336}K^{337}$) corresponding to the abovementioned phospho-accepting sites of DMI3. This variant only partially complements the *M. truncatula dmi3-1* mutant, leading to the formation of nodule-like structures that lack rhizobia colonization and are therefore unable to establish a functional symbiosis (Godfroy et al. 2006). We further compared the protein sequences of 221 DMI3 homologs retrieved from the NCBI (https://www.ncbi.nlm.nih.gov/)

Downloaded from academic.oup.com/plphys/article/202/2/kiag347/8704448 by Hangzhou Normal University user on 03 November 2026

(Table S2). Interestingly, DMI3 homologs from Fabaceae, Cucurbitaceae, Rosaceae, and Fagaceae, which are known to practice RNS, all carry 3 residues able to accept phosphorate groups in this triplet (Figure S13). In contrast, in DMI3 homologs from Poaceae, which are well known to be unable to practice RNS, carry no more than 2 phosphate-accepting residues within that triplet, and none of these have a last residue in the triplet accepting a phosphorate group (Figure S13). It seems that 3 phosphorate-accepting residues in this triplet at the end of CBD of DMI3s play a vital role in adequately supporting RNS.

We generated an OsCCaMK mutant by substituting the phosphoablative residues C336/K337 to generate the OsCCaMK^{C336SK337T} mutant. We then compared abilities of OsCCaMK^{C336SK337T}, wild-type OsCCaMK, and wild-type DMI3, to restore RNS in *dmi3-1* roots via hairy root transformation. Infected nodule formation was evaluated by examining transgenic roots or untransformed *dmi3-1* roots at 5 weeks post Rm1021 inoculation. We observed that nodulation on *dmi3-1* roots transformed with the *OsCCaMK^{SST}* was restored to a similar level as that in *dmi3-1* roots transformed with *DMI3*. Although nodular structures formed on *dmi3-1* roots transformed with OsCCaMK^{SCK}, these structures remained white and spherical, indicating that rhizobial infection was unsuccessful (Figs. 6a~c). In *dmi3-1* roots expressing *DMI3^{SST}* or *OsCCaMK^{SST}*, rhizobia successfully colonized the inner cortical cells of nodules, indicating that these constructs restored normal rhizobial infection. Additionally, there was no significant difference in the fresh weight of shoots between *dmi3-1* plants their roots transformed with *DMI3^{SST}* or *OsCCaMK^{SST}*, although both showed significantly higher shoot weights compared to plants with *dmi3-1* roots transformed with *DMI3^{SCK}*. Similarly, no significant difference was observed in the fresh weight of roots between plants with *dmi3-1* roots transformed with *DMI3^{SST}* or *OsCCaMK^{SST}*, but both had significantly higher root weights than those with *dmi3-1* roots transformed with *DMI3^{SCK}* (Figs. 6d, e). Determination of nitrogenase activity in nodules transformed with *OsDMI3^{SCK}* revealed significant differences compared to other constructs. Specifically, nitrogenase activity in nodules transformed with *OsDMI3^{SCK}* was reduced by approximately 84% compared to those transformed with *MtDMI3^{SST}*, and by approximately 83% compared to those transformed with *OsDMI3^{SST}* (Fig. 6f).

Using the GST pull-down assays, we found that OsCCaMK^{SCK} almost does not interact with MtIPD3 (Figure S14). However, when the wild-type OsCCaMK^{SCK} was mutated to OsCCaMK^{SST}, it gained an affinity to MtIPD3 (0.87) similar to that (1.0) exhibited by DMI3^{SST} (Figure S14). Further in vitro kinase assays, coupled with mass spectrometry analysis, revealed that wild-type OsCCaMK^{SCK} showed a lower level of phosphorylation on MtIPD3 than DMI3 (Table S3). Additionally, there were significant differences in the locations of phosphorylation sites on IPD3 phosphorylated by OsCaMK^{SCK} (T82 and S88) and DMI3^{SST} (S13, T33, S43, S77, S81, S97, T163, S168, S176, and S445) (Table S3). These results suggest that the partial complementation of the *dmi3-1* mutant by OsCCaMK^{SCK}, along with the observed defects in nodule development, may be related to its impaired interaction with MtIPD3 and the altered phosphorylation pattern of MtIPD3.

To test the functional conservation of C-terminal phosphorylation residues in DMI3, we generated transgenic lines in the *dmi3-1* mutant background (Fig. 6g). The *dmi3-1* plants were transformed with either the wild-type DMI3 (DMI3^{SST}), the rice *OsCCaMK* carrying the SST substitution (OsCCaMK^{SST}), or the rice *OsCCaMK* carrying the *SCK* substitution (OsCCaMK^{SCK}).

As shown in Fig. 6h, the number of rhizobial-infected nodules per plant was significantly higher in DMI3^{SST} and OsCCaMK^{SST} lines compared to OsCCaMK^{SCK} lines. Specifically, DMI3^{SST} and OsCCaMK^{SST} supported an average of 8 to 9 infected nodules per plant, whereas OsCCaMK^{SCK} only formed 3 to 4 infected nodules.

To assess the temporal dynamics of symbiotic gene expression, we measured the relative expression of a key symbiosis marker at 1, 2, 3, and 4 wpi in the OsCCaMK^{SST} (Fig. 6i). The expression level increased steadily from 1 to 3 wpi, reaching a peak at 3 wpi, and then slightly declined by 4 wpi.

Consistent with the nodulation data, the expression of *MtNIN* was significantly higher in DMI3^{SST} and OsCCaMK^{SST} lines than in OsCCaMK^{SCK} lines (Fig. 6j). OsCCaMK^{SST} lines showed an approximately 5.4-fold increase in *MtNIN* expression relative to OsCCaMK^{SCK} lines, and a comparable level of *MtNIN* expression to DMI3^{SST} lines.

Collectively, these data support the conclusion that the C336S/K337T substitution restores CCaMK function to a level capable of supporting both nodule organogenesis and MtNIN expression during root nodule symbiosis (RNS). These findings reinforce the view that the triple phosphorylation residues at the C-terminus of the DMI3-Ca^{2+}/calmodulin-binding domain (CBD) play an essential role in the efficient establishment of rhizobial symbiosis.

AlphaFold 3 predicted structural basis of phosphorylation-driven CBD conformational cascade regulating DMI3 dual functions.

Using AlphaFold 3 (Abramson et al. 2024), we modeled the DMI3-CaM-IPD3 complex in 3 distinct phosphorylation states: the non-phosphorylated state (SST), the singly phosphorylated state at T345 (hereafter T345p), and the triple-phosphorylated state at S343, S344, and T345 (hereafter S343p/S344p/T345p). The predicted structures revealed a phosphorylation-driven conformational cascade within the calmodulin-binding domain (CBD) that underpins the DMI3 functional switch. In the SST state, the CBD adopts a compact conformation that stabilizes the ternary complex, sequestering IPD3 in an inactive conformation that is consistent with a scaffold function (Figure S15a). Upon single phosphorylation at T345 (T345p), the CBD undergoes local rearrangement that exposes S343 and S344 while preserving overall complex integrity, representing an intermediate primed state (Figure S15b). Progressive triple phosphorylation (S343p/S344p/T345p) triggers pronounced relaxation of the CBD, disrupting both CaM binding and the CBD-kinase domain interface, leading to complex disassembly and kinase activation (Figure S15c). This cascade directly modulates DMI3 kinase activity: the compact CBD in SST and T345p maintains autoinhibition, whereas triple phosphorylation relieves autoinhibition, promoting both auto-P and phosphorylation of its substrate IPD3. Together, these structural insights provide a mechanistic framework for understanding how triplet phosphorylation coordinates the transition from the DMI3 scaffold function (SST) to its kinase-active state (S343p/S344p/T345p) during root nodule symbiosis.

Discussion

DMI3 is activated by intracellular calcium oscillations triggered by Nod-factor. As a decoder of Ca^{2+} signals, DMI3 activities in both auto- and sub-P are orchestrated by Ca^{2+} signal readouts via its own EF-hands and/or calmodulin inside the nucleus (Patil et al. 1995; Takezawa et al. 1996).

The interplay between DMI3/CCaMK, CaM, and IPD3/Cyclops in rhizobial nodulation symbiosis involves a complex regulatory network.

Downloaded from academic.oup.com/plphys/article/202/2/kiag347/8704448 by Hangzhou Normal University user on 03 November 2026

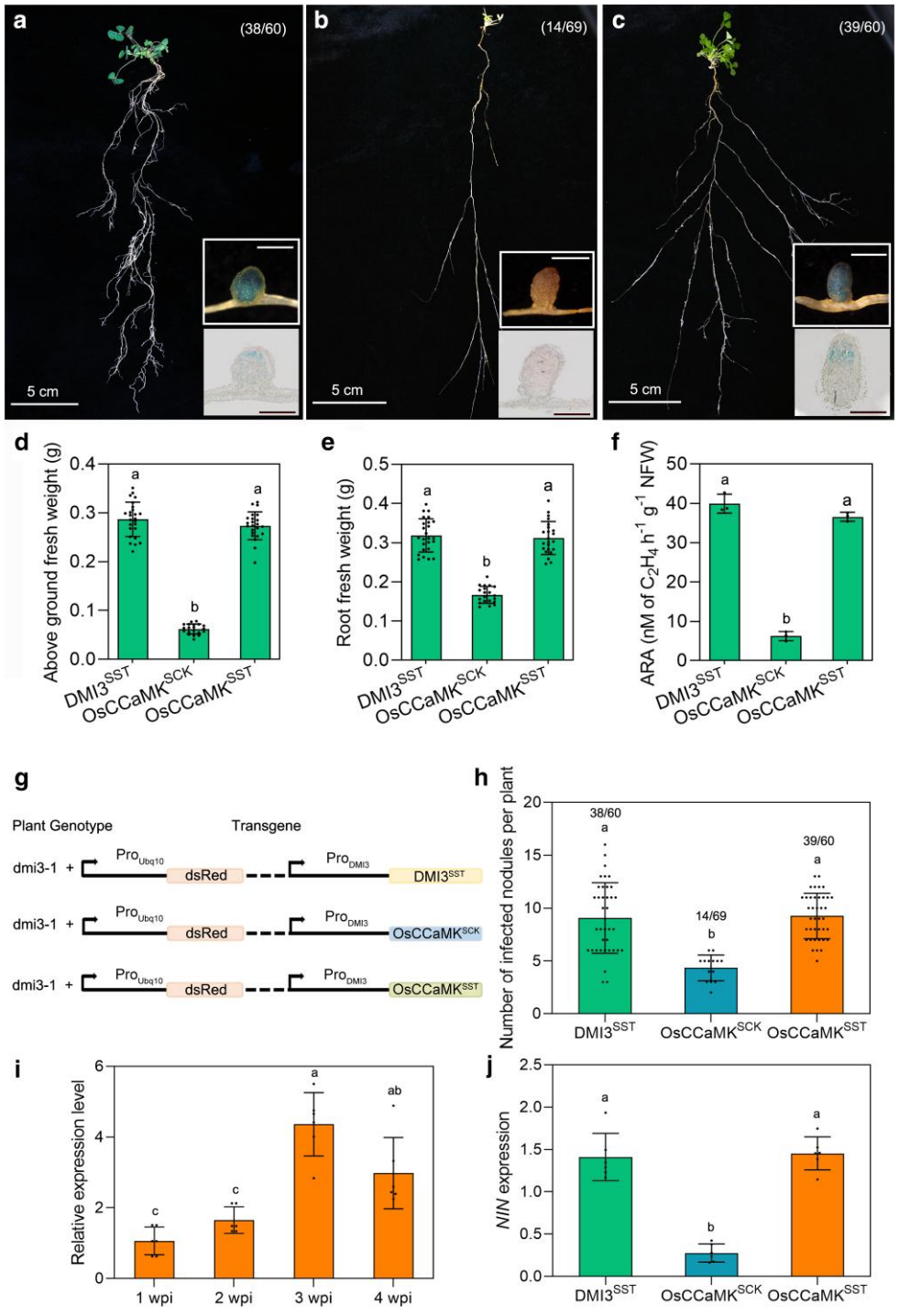


Figure 6 The site mutated rice OsCCaMK (from *OsCCaMK*^{SCK} to *OsCCaMK*^{SST}) restores nodulation of *Medicago truncatula dmi3-1* mutant. (a) The *dmi3-1* mutant roots transformed with *DMI3*^{S343S344T345} (*DMI3*$^{SST(WT)}$). */*, number of infected nodulating plants/total tested plant. (b) The *dmi3-1* mutant roots transformed with *OsCCaMK*^{S335C336K337} (*OsCCaMK*^{SCK}). */*, number of uninfected nodulating plants/total tested plant. (c) The *dmi3-1* mutant roots transformed with *OsCCaMK*^{S335S336T337} (*OsCCaMK*^{SST}). */*, number of infected and uninfected nodulating plants/total tested plant. The transgenic hair roots were infected with *Sinorhizobium meliloti* Rm1021 (carrying the *hemA::LacZ* construct). 5 weeks post inoculation, the nodules were collected and stained with X-gal solution. Scale bar, 5 cm (main panel); scale bar in the inset, 1 mm. (d) and (e) The *dmi3-1* mutant roots transformed with *DMI3*^{SST}, *OsCCaMK*^{SCK} or *OsCCaMK*^{SST} and infected with *Sinorhizobium meliloti* Rm1021 (carrying the *hemA::LacZ* construct). Fresh weight of above-ground of plants and fresh weight of roots were recorded after 5 weeks of inoculation. All data are means ± SE ($n \geq 25$). (f) Acetylene reductase assay (ARA). NFW, nodule fresh weight. All data are means ± SE ($n = 3$). (g) A schematic structural depiction of plasmids for hairy root transformation. (h) Root nodule numbers on *dmi3-1* roots transformed with OsCCaMKSCK or OsCCaMKSST were evaluated 5 wpi. Data are means ± SE ($n \geq 60$). (i) Expression analyses of MtNIN in *dmi3-1* transformed with OsCCaMKSST by real-time PCR at 1, 2, 3 and 4 wpi. Values are means ± SE ($n = 6$). (j) Transcriptional expression of MtNIN gene in *dmi3-1* roots transformed with DMI3SST, OsCCaMKSCK, and OsCCaMKSST 3 wpi. The relative expression level was normalized against that of the M. truncatula ubiquitin. Data are means ± SE ($n = 6$). Different letters represent significant differences [$P < 0.05$ by one way analysis of variance3 with Waller-Duncan *k*-ratio *t*-test].

Downloaded from academic.oup.com/plphys/article/202/2/kiag347/8704448 by Hangzhou Normal University user on 03 November 2026

DMI3, activated by intracellular calcium oscillations, interacts with CaM and IPD3 to initiate the symbiotic signaling cascade. CaM plays a pivotal role in enhancing both the auto-P of DMI3 and the phosphorylation of its substrate, MtIPD3, both of which are critical for proper activation of downstream signaling cascade (Yano et al. 2008). However, CaM also modulates the interaction between CCaMK and Cyclops, which is crucial for the proper activation of RNS (Liao et al. 2012). This dual action of CaM suggests a finely tuned regulatory mechanism, in which CaM modulates DMI3 activity and its interaction with IPD3, thereby controlling the symbiotic signaling pathway. Interestingly, this study showed that the kinase activities of almost all phosphomimic mutants at S343, S344, and T345 remain responsive to CaM in both auto- and sub-P, despite most of these mutants no longer interacting with CaM (Figs. 2 and 3). Similar findings were observed in studies involving LjCCaMK^{S337D} and DMI3^{S344D} mutants (Liao et al. 2012; Routray et al. 2013). Evidently, the kinase activities of these DMI3 phosphomimic mutants, except DDD, could still be modulated by CaM, albeit with altered responsiveness. These findings are similar to those of Jauregui et al. (2017), who discovered that the S343D and S344D mutations did not inhibit the interaction between the CBD peptide and CaM but did abolish the binding of CaM to the full-length DMI3 (Jauregui et al. 2017). A possible explanation is that although CaM cannot form a stable interaction with DMI3^{S343D} or DMI3^{S344D}, it might still form transient and unstable complexes with their CBD segments, thereby influencing the kinase activities of DMI3. Nonetheless, this hypothesis warrants further investigation.

DMI3 has been shown to interact with and phosphorylate IPD3 at multiple residues, including S50 and S155, to activate the expression of *NIN*, an essential player for the establishment of RNS (Singh et al. 2014; Jin et al. 2018). This is further supported by the observation that any phosphomimic mutation at the triplet in CBD of DMI3, which prevents its interaction with IPD3, fails to support the establishment of RNS (Liao et al. 2012; Routray et al. 2013). Our study corroborates these findings, confirming that the interaction between DMI3 and IPD3 is essential for RNS activation (Singh et al. 2014). However, we have revealed an additional aspect of this interaction: DMI3 must dissociate from activated IPD3 to effectively regulate the transcription of the *NIN* gene. Previous work proposed that *NIN* expression is activated by the CaM-DMI3-IPD3 complex (Singh et al. 2014), and our current results showed that the dissociation of these complexes is a crucial step in RNS activation. This dissociation enables the release of phosphorylated IPD3, which in turn initiates the downstream transcriptional cascade. Together, our findings provide insights into the dynamic nature of the DMI3-IPD3 interaction and its role in regulating *NIN* expression during RNS.

Our identification of a nonpalindromic *IPD3-RE$_{NIN}$* offers an alternative perspective to the canonical model proposed by Singh et al. (2014), in which Cyclops binds DNA exclusively as a homodimer to palindromic sequences. This finding suggests evolutionary divergence in DNA recognition mechanisms within the IPD3/Cyclops protein family. Future structural studies, particularly high-resolution comparative analyses of IPD3 or IPD3^{DD} in complex with the nonpalindromic *IPD3-RE$_{NIN}$*, will be essential to validate this hypothesis and elucidate the molecular mechanisms underlying its binding versatility.

The regulatory mechanism of DMI3 in RNS is complex, involving both positive and negative regulatory roles. Knockout or kinase-dead mutations in DMI3 result in the loss of RNS function, highlighting its positive regulatory role (Catoira et al. 2000; Tirichine et al. 2006; Miller et al. 2013). Regarding DMI3 auto-P, our study reveals a dual function, with both negative and positive regulatory capacities. Previous studies have shown that auto-P at the T271 residue acts as a negative regulator, preventing spontaneous nodulation, and potentiating its responding to signal conveyed by Ca^{2+}/CaM (Miller et al. 2013). Additionally, any phosphomimic mutation within the $S^{343}S^{344}T^{345}$ triplet deactivates DMI3, impairing its ability to support RNS. These findings suggest that auto-P at this site serves as a negative regulatory mechanism. Moreover, we demonstrate that phosphorylation at any residue within the $S^{343}S^{344}T^{345}$ triplet promotes further auto-P within the triplet itself, acting as a positive regulator. This auto-P also likely activates DMI3 kinase activity, enabling the phosphorylation and activation of IPD3. Concurrently, increased phosphorylation at the $S^{343}S^{344}T^{345}$ triplet facilitates the dissociation of the CaM-DMI3-IPD3 complex, releasing the activated IPD3 to initiate RNS.

Given the complexity of the DMI3-IPD3 interaction and its role in RNS activation, it is important to consider the nature of the kinase-substrate interaction itself. Apparently, a stable physical interaction between a kinase and its substrate is not required for the phosphorylation reaction to take place (Ouyang et al. 2010; Kim and Hwang 2011; Routray et al. 2013; Ito et al. 2017). Similar situations have been observed in in vitro kinase assays of many Ser/Thr kinases, including DMI3, CaPIK1, OsSIK1, and NtCDPK1, with the use of bovine myelin basic protein (MBP) as a universal substrate. Although MBP is generally used as an ideal substrate for numerous Ser/Thr kinases, it does not stably interact with all of these kinases. A reasonable speculation might be that kinase phosphorylation of substrate occurs instantaneously even though the 2 proteins contact each other only transiently, and this transient contact is different from stable protein-protein interaction, which usually results in the formation of a stable multiunit complex.

Considering that stable interaction is not required for DMI3 to phosphorylate IPD3, and documented results showed that DMI3 binding to IPD3 is required for proper development of RNS (Singh et al. 2014), one could reasonably speculate that DMI3 might act as a scaffold to hold MtIPD3 and expose specific residues for their trans-phosphorylation by a different copy of DMI3.

To release the phosphorylated MtIPD3, more than 2 residues within the $S^{343}S^{344}T^{345}$ triplet must be phosphorylated. A key question is which residue within the unphosphorylated $S^{343}S^{344}T^{345}$ triplet is preferentially phosphorylated first, and whether there is a sequential pattern to the autophosphorylation of these 3 adjacent residues. Considering that the T345D mutation only partially affects CaM binding of DMI3, while S343D or S344D mutation completely blocks DMI3 and CaM interaction, it is conceivable that, in the DMI3-CaM complex, S343 and S344 in DMI3 might be right within the docking site of CaM, while T345 is closely positioned outside the docking site. Therefore, T345 could be the first residue to be autophosphorylated, facilitating the exposure of S344 and S343 for sub-P, which effectively separates CaM from DMI3. Similarly, considering that the S343D mutation only partially affects IPD3 binding to DMI3, whereas the S344D or S345D mutation complete blocks IPD3 and DMI3 interaction, it is likely that S344 and S345 are right within the docking site of IPD3, while T343 is closely positioned outside the docking site. The phosphorylation of S343 would help expose S344 and T345 for sub-P, which effectively separates IPD3 from DMI3. In short, the phosphorylation of T345 and S343 serve as key roles in releasing CaM and MtIPD3 from DMI3-CaM and DMI3-MtIPD3 complexes, respectively.

Considering the rigidity of the kinase and the fact that auto-P of DMI3 happens at multiple positions in DMI3, it is difficult to conceive

Downloaded from academic.oup.com/plphys/article/202/2/kiag347/8704448 by Hangzhou Normal University user on 03 November 2026

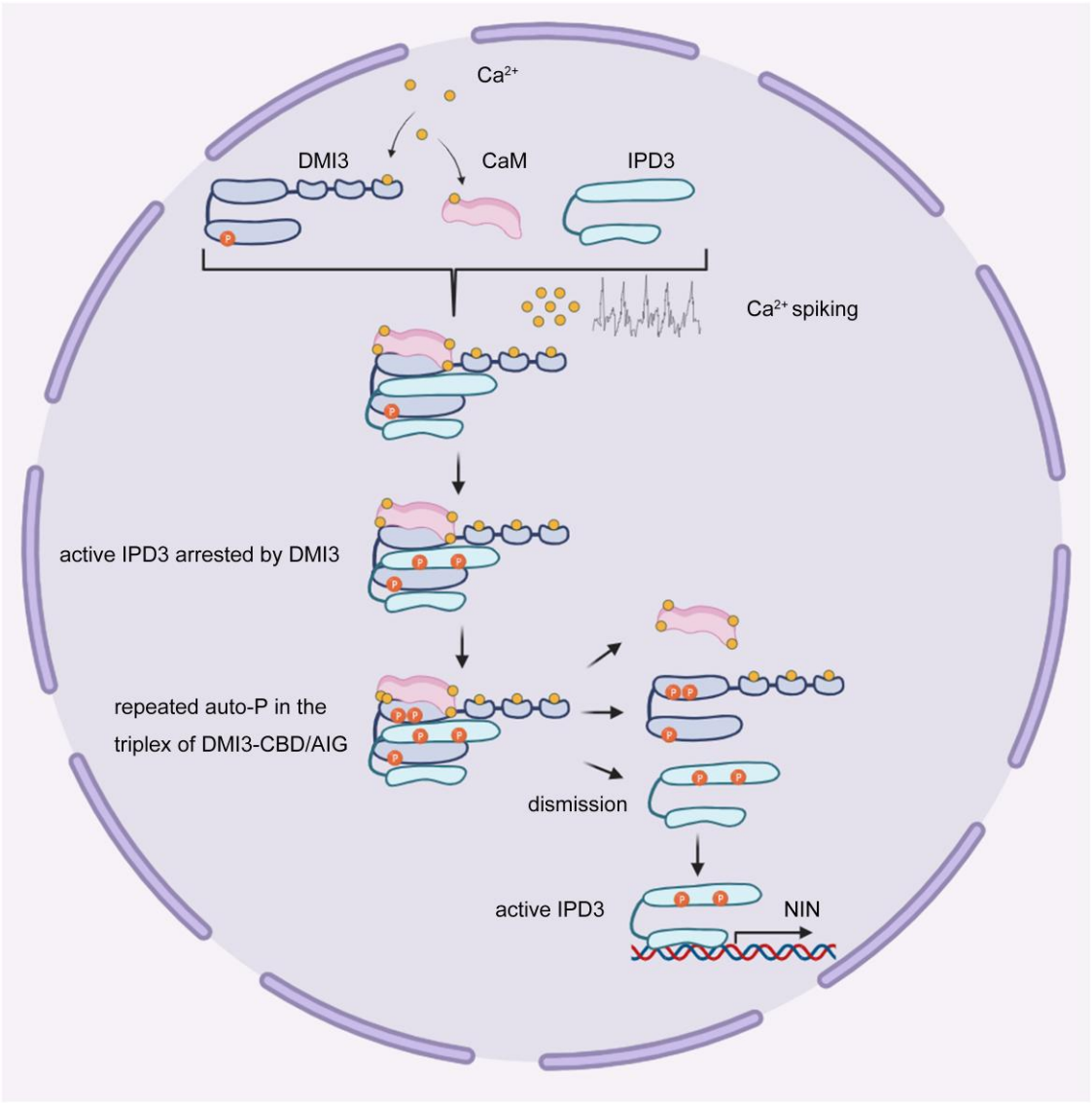


Figure 7 A working model for the role of CaM-DMI3-IPD3 in regulating root nodulation symbiosis in *Medicago truncatula*. In the resting condition, Ca^{2+} binding to at least 1 of the 3 EF-hands, preferably the 3rd DMI3, is required to trigger a conformational change and leading to autophosphorylation of T271. It is unclear whether calmodulin (CaM) is fully loaded with Ca^{2+} under resting conditions, but it is likely not, meaning that CaM cannot yet bind to DMI3, and the Ca^{2+}/CaM-DMI3-IPD3 complex does not form at this stage. Considering DMI3 and IPD3 can interact without involvement of Ca^{2+}/CaM, the DMI3-IPD3 may form at the resting condition. Upon rhizobium stimulation, Ca^{2+} spiking occurs in the nucleus, fully loading CaM with Ca^{2+} and facilitating the formation of Ca^{2+}/CaM-DMI3-IPD3 complex. Ca^{2+}/CaM binding to DMI3 override the T271 phosphorylation triggered sealing on DMI3's kinase activities and enable it to phosphorylate IPD3 as well as undergo autophosphorylation. Phosphorylation of IPD3 will enable it to bind to its target gene promoter, while DMI3 will be phosphorylated at its $S^{343}S^{344}T^{345}$ triplex residues. This autophosphorylation disrupts the CaM-DMI3-IPD3 complex and release the activated IPD3 to trigger the downstream *NIN* transcriptional cascade. Although DMI3, CaM, and MtIPD3 are all essential components in RNS, our findings support the role of activated MtIPD3 as a player separated from DMI3 to bind the cis-element of *NIN* and induce its transcription.

that the phosphorylation is carried out in a cis-action manner—ie, a single DMI3 molecule phosphorylates itself at multiple positions. Instead, trans-action phosphorylation of DMI3 is a more reasonable and practical alternative, in which 1 DMI3 is phosphorylated by another nearby DMI3. Furthermore, the regulatory role of the triplet phosphorylation residues within DMI3 in the context of symbiotic interactions is also worth exploring. Since arbuscules form normally in the *MtIPD3*&*MtIPD3*-like double knockout mutant (*ipd3l*&*ipd3-2*) (Jin et al. 2018; Lindsay et al. 2019), it is unlikely that the regulatory mechanism of the triplet phosphorylation residues in DMI3, which governs the CaM-DMI3-IPD3 complex, is essential for symbiotic interactions with arbuscular mycorrhizal fungi in legumes. The regulatory role of the triplet phosphorylation residues within DMI3 on the CaM-DMI3-IPD3 complex may not be involved in the symbiotic interactions with arbuscular mycorrhizal fungi in leguminous plants. Since a loss-of-function mutation of DMI3 can shut down arbuscular mycorrhizal symbiosis (AMS) (Lévy et al. 2004; Gleason et al. 2006; Takeda et al. 2012), some unknown components downstream of DMI3, as well as additional regulatory mechanisms, likely play significant roles during arbuscular mycorrhizal symbiosis.

While not objecting to the essential role of the CaM-DMI3-IPD3 complex in activating RNS, the current research significantly

Downloaded from academic.oup.com/plphys/article/202/2/kiag347/8704448 by Hangzhou Normal University user on 03 November 2026

advanced our understanding of how the DMI3 and IPD3 interplay activates RNS. Functional complementation data shown in Fig. 1 demonstrate that DMI3 need to transition from a phosphorylation-free condition to a status in which at least 2 of these 3 residues in the CBD triplet are phosphorylated during the normal activation process of RNS (Figs. 1b, c and d). Our results further support the finding that the DMI3 molecule itself is an arrester of the activated IPD3, which keeps its function on hold (Figs. 4e, f). Repeated phosphorylation in the triplet at the end of DMI3 CBD would likely dismiss the CaM-DMI3-IPD3 complex and releases the activated IPD3 to kick off the establishment of RNS, as phosphomimic mutations in the triplet break the interaction between DMI3 and IPD3.

Conclusions

Together with documented results, our data support a hypothesis (Fig. 7) that the Ca^{2+} signal triggering the activation of DMI3-IPD3 pathway during RNS is not a simple on and off action, it includes a series of events in the following rough order: 1) Ca^{2+} binding to EF-hands of DMI3, which has a very low Kd to Ca^{2+}, to trigger T271 phosphorylation at rest condition (Miller et al. 2013); this seals the activities of DMI3 and suppresses spontaneous nodulation, and also potentiates it for binding to CaM, which has a significantly higher Kd to Ca^{2+}; 2) DMI3 binds to CaM in a Ca^{2+} excited condition and recruits IPD3 to the complex, suggesting that the interaction between DMI3 and IPD3 could happen before CaM-binding, even in stage 1; 3) CaM-binding to CBD of DMI3 overrides autoinhibition and enables the phosphorylation of IPD3 at the right positions, changing IPD3 to an activated status but arresting it in the complex to keep it nonfunctional; 4) repeated auto-P of DMI3 in the $S^{343}S^{344}T^{345}$ triplet dismissed the complex, releasing the phosphorylated and activated IPD3 to activate the RNS transcriptional cascade.

Materials and methods

Plant materials and symbiotic inoculation

The seeds of the Medicago (*Medicago truncatula*) wild-type accession A17 and the *dmi3-1* mutant were scarified and surface sterilized with 1.75% sodium hypochlorite solution. Sterilized seeds were imbibed and vernalized in sterile distilled water for 24 h at 4 °C before germination on nitrogen-free Fahräeus agar plate (Cerri et al. 2017). The composite plants with transformed roots were generated as described in the *Medicago truncatula* handbook, with minor modifications. Briefly, approximately 3 mm of radicles from the root tip were cut the day after germination. The sectioned surfaces were coated with *Agrobacterium rhizogenes* strain K599 and were then transferred onto a Fahräeus agar plate at 22 °C under a 16-h-light/8-h-dark photoperiod. After 4 days, the plants were transferred onto a Murashige and Skoog plate containing 100 mg/L cefotaxime (Kang et al. 2011) until the hairy roots reached an average of 4∼5 cm. The transformed roots were selected based on constitutive expression of the red fluorescent marker protein (DsRED).

For root nodule symbiosis, the composite seedlings were transplanted in open pots containing a 1:1 ratio of vermiculite and perlite mixture, saturated with nitrogen-free Fahräeus solution at 21 °C under a 16-h-light/8-h-dark photoperiod (Jin et al. 2018). Root nodule formation was induced using *Sinorhizobium meliloti* Rm1021 harboring the *hemA::LacZ* construct (Routray et al. 2013) or the GFP-labeled strain Sm2011-GFP which was kindly provided by Professor Ertao Wang at the Center for Excellence in Molecular Plant Sciences, Chinese Academy of Sciences. Infected nodules were observed 5 to 8 wpi (Godfroy et al. 2006; Cerri et al. 2017), while spontaneous nodules were counted 8 weeks after transplanting in pots without rhizobia (Jin et al. 2018). The infected nodules were verified by X-gal (5-Bromo-4-chloro-3-indolyl-beta-D-galactopyranoside) staining as described by Jarzyniak et al. (Jarzyniak et al. 2021). Each independent experiment contained at least 10 plants per genotype.

Site-directed mutagenesis

The mutated variants were achieved using the Mut Express MultiS Fast Mutagenesis Kit V2 (Cat NO. C215-01, Vazyme, Nanjing, China) according to the manufacturer's instructions. The synthesis of DNA oligonucleotides and sequencing of mutated plasmids were conducted in Tsingke Biotechnology Co. Ltd (Beijing, China). The sequences of DNA oligonucleotides used in mutagenesis are listed in Table S4.

Plasmid construction

For complementation of the *M. truncatula dmi3-1* mutant, the coding sequences of *Oryza sativa CCaMK* wild type (*OsCCaMK*^{S335C336K337} or *OsCCaMK*^{SCK}) and its mutant (*OsCCaMK*^{S335S336T337} or *OsCCaMK*^{SST}), *DMI3/MtDMI3* and its mutants (Table S5) were inserted into the *pDL28_DPR* vector (a derivative of pCAMBIA1300 incorporated with an *ubq10::DsRed* expression cassette and a DMI3 promoter (Du et al. 2009) by *Kpn* I site under the control of the native *DMI3* promoter (Routray et al. 2013).

For the tobacco (*Nicotiana benthamiana* L.) leaves transformation system, the full-length coding sequence of *DMI3* and 14 site-mutants (with stop codon) were introduced into the pCAMBIA1300 vector via *Xba* I restriction sites, resulting in the construct *pCAMBIA1300-35S-DMI3s*, with the DMI3 and 14 site-mutants positioned downstream of the 35S promoter. Similarly, the coding sequence of *MtIPD3*^{DD} (free of stop codon) was inserted into the pCAMBIA1300 vector by *Sac* I and *Sal* I sites generate *pCAMBIA1300-35S-MtIPD3*^{DD}, with *MtIPD3*^{DD} also positioned downstream of the 35S promoter. In addition, the promoter of *MtNIN* (P_{MtNIN}) (in Note S1, Jin et al. 2016) and *IPD3-RE*$_{NIN}$ free mutant (mP_{MtNIN}) was inserted into pCAMBIA1300NH-GUS by *Kpn* I and *Xba* I, and forming a P_{MtNIN}*::GUS* unit in this vector (defined as *pCAMBIA1300NH-*P_{MtNIN}*-GUS*). To analyze the impact of phosphomimic or phospho-ablative mutations within the DMI3 triplet on the activation of MtNIN by MtIPD3, we employed a strategic molecular cloning approach. Specifically, the P_{MtNIN}*::GUS* construct was PCR-amplified and subsequently introduced into the previously described pCAMBIA1300-35S-MtIPD3^{DD} vector using the *AsiS* I restriction site. This precise cloning technique facilitated the generation of a binary vector, designated as *pCAMBIA1300-35S-MtIPD3*^{DD}*-*P_{MtNIN}*::GUS*, which serves as a critical tool for our investigation.

To generate prokaryotic expression vectors, the coding sequence of *DMI3* and *Arabidopsis thaliana calmodulin 2* (*AC2*) (coding for a calmodulin protein which with 100% sequence identity of *Medicago truncatula* calmodulin [GenBank: RHN66621.1]) were inserted into the pET28a vector by *Xho* I and *Nde* I sites, and fused with a C-terminal His-tag. The primer pairs DMI3-Nhe1-F/DMI3-Xho1-R and AtCaM2-F/R (Table S5) were used for amplifying *DMI3* and *AC2* in the abovementioned process.

To assay the interaction between DMI3s and MtIPD3 in yeast, full-length *DMI3* and its site-mutants were fused to the GAL4 DNA binding

Downloaded from academic.oup.com/plphys/article/202/2/kiag347/8704448 by Hangzhou Normal University user on 03 November 2026

domain (BD) by *Sal* I and *Pst* I in the pBD-GAL4 Cam vector, and the *MtIPD3* CDS was fused to the GAL4 DNA activation domain (AD) by *BamH* I and *Xho* I in the *pAD-GAL4-2.1* vector, so as to form *pBD-GAL4 Cam-DMI3s* and *pAD-GAL4-2.1-MtIPD3* vectors, respectively. In order to evaluate the effect of calmodulin on the binding efficiencies between DMI3s and MtIPD3, the P_{ADH1}::*AC2* expression unit was additionally inserted into the *pAD-GAL4-2.1-MtIPD3* vector, forming a *pAD-GAL4-2.1-MtIPD3&AC2 vector*. Briefly, the *ADH1* promoter, *AC2* CDS and *ADH1* Terminator were amplified by pAD-AC2-F1/R1, pAD-AC2-F2/R3 and pAD-AC2-F3/R3 primer pairs (Table S5), respectively, and inserted into the *pAD-GAL4-2.1-IPD3* vector which was predigested by *Aat* II.

Microscopic observation

Entire root nodules were stained with 5-bromo-4-chloro-3-indolyl-β-d-galactoside (X-gal) and observed under a light microscope as described in Jarzyniak et al. (2021). Root nodules inoculated with Rm1021 carrying a Lac Z reporter were fixed in 2% (v/v) glutaraldehyde solution for 1 h at room temperature, rinsed 3 times in Z′ buffer consist of 0.1 M potassium phosphate buffer pH 7.4, 1 mM $MgSO_4$, and 10 mM KCl, and stained in Z′ buffer containing 0.08% X-gal, 5 mM $K_3Fe(CN)_6$, and 5 mM $K_4Fe(CN)_6$ for 12 h at 28°C. The nodules were then destained in 2.5% solution of sodium hypochlorite and observed under a stereo microscope (Nikon SMZ1270).

Nodule sections were stained with X-gal or toluidine blue as described in Jarzyniak et al. (2021) and Routray et al. (2013), respectively, with a few modifications. Fresh root nodules were fixed overnight in 70% FAA (consists of 1.33% formalin, 3.5% acetic acid, and 44.1% alcohol) at room temperature (RT). The fixed nodules were soaked in Plant Softening Solution (Cat NO. G1115, Servicebio, Wuhan, China) for 1 wk at 55 °C. The softened nodules were dehydrated in an ethanol series (30, 50, 75, 85, 90, 95, and 100% ethanol, each for 1.5 h) and embedded in Technovit 7100 (Heraeus Kulzer, Hanau, Deutschland) according to the manufacturer instructions. The embedded nodules were sliced into 14-μm-thick longitudinal sections using a Leica RM2016 microtome and stained for 1.5 min in 0.05% (w/v) toluidine blue. The sections were analyzed using a Nikon Eclipse Ti microscope, and representative images were obtained using a Digital Sight DS-U3 camera (https://www.microscope.healthcare.nikon.com/).

Yeast 2-hybrid (Y2H) assay

Y2H analysis was performed using the HybriZAP-2.1 XR System (Cat No. 235612 Agilent Technologies Inc, California, USA) according to the manufacturer protocol. The *pBD-GAL4-Cam-DMI3s* and *pAD-GAL4-2.1-MtIPD3* constructs were cotransformed into the yeast strain YRG2 (Cat NO. 240060, Agilent Technologies Inc). These transformants were screened on SD selective plates lacking leucine, histidine, tryptophan and uracil. The interaction intensities were determined by β–galactosidase quantitative assays as described by Routray et al. (2013). Over six independent colonies for each of the constructs were tested.

Transactivation assay in *N. benthamiana* leaves

For tobacco leaves transformation system, the P_{DMI3}::*DMI3*s and *pCAMBIA1300-35S-IPD3*^{DD}-P_{MtNIN}::*GUS* or *pCAMBIA1300-35S-IPD3*^{DD}-P_{MtNIN}::*GUS* constructs were introduced into 4-week-old tobacco leaves using *Agrobacterium tumefaciens* strain GV3101 as described previously (Liu et al. 2021).

GUS reactions were performed in GUS-staining solution containing 1 mM X-Gluc, 0.5 mM potassium ferrocyanide, 5 mM Na_2EDTA, and 0.1 M phosphate buffer (pH 7.0). Root nodules or tobacco leaves were vacuum infiltrated with the abovementioned GUS-staining solution overnight at 37 °C in the dark. The enzymatic reaction was stopped by replacing the GUS solution with 100% ethanol before microscopy observations.

To evaluate how phosphomimic or phosphoablative mutations at the C-terminus of CaMBD in DMI3 affect the activation of MtNIN promoter by MtIPD3, *MtNIN* promoter as used by Jin et al. (2016). fused to the *uid A* gene (P_{MtNIN}::*GUS*), was coexpressed together with activated *MtIPD3*^{DD} with or without *DMI3* and its mutated versions in *N. benthamiana* leaf cells. The transactivation of the reporter constructs was quantified by fluorometric GUS assay (MUG assay) as described by Cervera (2005), with slight modifications. In brief, 100 mg transformed tobacco leaves were homogenized in liquid nitrogen. The powders were transferred into 400 μL of extraction buffer (50 mM sodium phosphate buffer, pH 7.0, 10 mM ethylenediaminetetraacetic acid disodium salt (EDTA-2Na), pH 8.0, 0.1% Triton X-100, 10 mM β-mercaptoethanol) and incubated for 15 min at 4 °C. The unlysed cells and debris were removed by centrifugation at 13,000 g for 10 min at 4 °C. The protein content in the supernatant was quantified by Bradford solution, and 80 μg total proteins and 2 mM 4-MUG substrate were added into abovementioned extraction buffer (total volume of 400 μL) at 37 °C in the dark. 100 μL of reaction mixtures at 3 different times (eg, 10, 20, and 30 min) were taken out and mixed immediately with 900 μL of Na_2CO_3 to stop the enzymatic reaction. The product of MU was measured by a Bio-Rad DNA fluorometer model TKO 100 with a fixed excitation bandpass source (365 nm) and an emission (460 nm) bandpass filter. For each sample, 3 fluorescence values corresponding to different reaction times were measured. The enzymatic activity of β-galactosidase was expressed as the slope of the amount of product formed in the reaction vs time (nmol of MU/min/μg of total protein).

Western blot analysis

Protein levels of DMI3 and IPD3-myc were quantified using anti-DMI3 and anti-myc antibodies, respectively, following the procedure described by Zheng et al. (2024). Briefly, 100 mg of *N. benthamiana* leaf tissue was ground to a fine powder in liquid nitrogen and homogenized in an extraction buffer containing 20 mM Tris-HCl (pH 7.5), 20 mM KCl, 2 mM EDTA, 2.5 mM $MgCl_2$, 25% glycerol, 250 mM sucrose, 5 mM DTT, and 10 mM protease inhibitor. The homogenate was briefly centrifuged, and the supernatant was collected as the total protein extract. For each sample, 20 μg of total protein was separated by SDS-PAGE and subsequently transferred onto a PVDF membrane using a wet blotting system. The membrane was blocked for 2 h at room temperature in blocking buffer (20 mM Tris–HCl, pH 7.5, 500 mM NaCl) containing 5% (w/v) nonfat dry milk (Beyotime, Cat No. P0216). After blocking, the membrane was incubated overnight at 4 °C with either an anti-Myc tag mouse monoclonal antibody (Sangon, Cat No. D191042) or an anti-DMI3 rabbit monoclonal antibody (generated in-house), each diluted at 1:5,000. Horseradish peroxidase-conjugated goat anti-mouse IgG (Sangon, Cat No. D111024) or goat anti-rabbit IgG (Sangon, Cat No. D111018) was used as the secondary antibody, with incubation for 1 h at room

Downloaded from academic.oup.com/plphys/article/202/2/kiag347/8704448 by Hangzhou Normal University user on 03 November 2026

temperature. Finally, immunoreactive bands were visualized using a multifunctional fluorescence imaging system (Bio-OI, Cat No. O1300) according to the manufacturer's instructions.

Expression and purification of *DMI3s* and *MtIPD3^{DD}*

DMI3 and its mutants were cloned into the bacterial expression vector pET28a (Cat No. 69864-3CN, Novagen) and transformed into *Escherichia coli* strain BL21 (DE3)/pLysS (Cat No. CD701-02, TransGen). The transformed bacteria were cultured in LB liquid media supplemented with kanamycin at 37 °C until the OD_{600} reached 0.3∼0.5. Recombinant protein expression was induced by adding 0.5 mM isopropyl β-D-1-thiogalactopyranoside (IPTG) and continued for 3 h. Cells were then harvested, lysed with lysozyme (1 mg/mL), and sonicated. The target proteins were purified using Ni–NTA agarose (Cat No. 30230, Qiagen) following the manufacturer protocol.

Similarly, MtIPD3^{DD} was expressed as an N-terminal GST-tagged fusion protein using the pGEX-6p-1 vector (Cat No. 28-9546-48, GE Healthcare) in *E. coli* strain BL21 (DE3). The expressed proteins were purified by affinity chromatography using GSTrap 4B (Cat No. 29048609, GE Healthcare) according to the manufacturer's instructions.

After purification, the proteins were dialyzed against a buffer containing 25 mM Tris/HCl (pH 7.6), 0.5 mM dithiothreitol, 1 mM EDTA, and 10 mM $MgCl_2$. Protein concentrations were determined using the Bradford reagent (Cat No. 5000201, Bio–Rad) with BSA as the standard. Finally, the purified proteins were stored at −80 °C in 15% glycerol for future use.

In vitro kinase assay

For the in vitro kinase assay of DMI3/OsCCaMK activity, 0.4 μg of DMI3s-His/OsCCaMKs-His was incubated in kinase buffer (25 mM Tris-HCl pH 7.6, 10 mM $MgCl_2$, 0.5 mM DTT, and 5 μCi [γ-^{32}P]-ATP) with either 5 mM ethylene glycol tetraacetic acid (EGTA) or 0.5 mM $CaCl_2$ and/or 1.0 μg Arabidopsis calmodulin 2 protein at 30 °C for 30 min. Bovine myelin basic protein (Cat No. M1891, Sigma-Aldrich, USA) or TrxA-MtIPD3-His was used as substrate. 1X SDS loading buffer was then added to stop the reaction. After separation by 12% SDS-PAGE, the phosphorylated DMI3 and MBP were visualized by autoradiography. Incorporation of radioactive phosphate was quantified using a liquid scintillation counter (MicroBeta^2 LumiJET, PerkinElmer Inc, Waltham, MA, USA).

Additionally, the phosphorylation sites of IPD3, phosphorylated by the kinases DMI3-SST and OsCCaMK-SCK, were further analyzed using mass spectrometry.

GST pull-down assay

The full-length CDS of MtIPD3 was subcloned into the pGEX-6P-1 vector to generate a GST-tagged fusion construct, while the full-length CDS of DMI3 and its mutant variants were inserted into the pET28a vector for the construction of C-terminal His-tagged fusion constructs. All recombinant plasmids were transformed into *Escherichia coli* BL21 (DE3) competent cells (CD601-02, TransGen Biotech, Beijing, China), and heterologous protein expression was induced with isopropyl β-D-1-thiogalactopyranoside (IPTG) under optimal conditions following standard prokaryotic expression protocols.

Recombinant MtIPD3-GST and DMI3 (or its mutant)-His fusion proteins were purified via GST Sepharose and Ni-NTA agarose affinity chromatography, respectively. The GST pull-down assay was performed to examine protein–protein interactions as previously described (Cao et al. 2025). Briefly, a mixture containing 2 μg of MtIPD3-GST (or GST), 5 μg of DMI3 (or its mutant)-His, 0 (or 0.5) μg of CaM, and 30 μL of GST beads (SA010005, Smart-Lifesciences, Changzhou, China) was incubated in binding buffer (50 mM Tris-HCl, pH 7.5, 150 mM NaCl, 1 mM EDTA) at 4 °C for 4 to 6 h to permit complex formation. The reaction mixture was further incubated at 4 °C for an additional 1 h with gentle rotation to capture the GST-tagged bait protein and its interacting partners.

Following incubation, the Glutathione Sepharose 4B beads were collected by centrifugation at 2,000 × g for 1 min and washed 6 to 8 times with a washing buffer consisting of 50 mM Tris-HCl (pH 7.5), 1 mM EDTA, 0.1% Triton X-100, and 10% glycerol to remove non–specifically bound proteins. The mixed bait and prey proteins (served as input samples) and the proteins retained on the beads were separated by SDS-PAGE. Subsequent immunoblotting analysis was performed using anti-His monoclonal antibody (M20020M, Abmart, Shanghai, China; 1:5000 dilution) and anti-GST monoclonal antibody (M20044F, Abmart, Shanghai, China; 1:5000 dilution) to confirm the specific interaction between MtIPD3 and DMI3 (or its mutants).

Microscale thermophoresis analysis

The cds of full-length MtIPD3^{DD}, in which both serine 50 (Ser50) and Ser155 were substituted with aspartic acid (Asp), was cloned into the *pGEX-6P-1* vector to generate an in-frame fusion with the GST tag. The resulting recombinant plasmid was transformed into *E. coli* BL21 (DE3) cells (CD601-02, TransGen Biotech, Beijing, China), and protein expression was induced by IPTG. The purified GST-tagged MtIPD3 protein was employed in microscale thermophoresis (MST) assays to evaluate its binding affinity toward 2 DNA ligands, CYC-RE and *IPD3-RE$_{NIN}$* (Table S6), following the methodology outlined by Ding et al. (2024). Prior to the assay, the GST-MtIPD3^{DD} protein was fluorescently labeled using RED-NHS dye (NanoTemper Technologies, MO-L011). Labeled protein was maintained at a constant concentration of 0.1 μM and incubated for 15 minutes at room temperature with each ligand, which was serially diluted from 20 μM to 0.61 nM in interaction buffer (1× PBST supplemented with 0.05% Tween-20). Measurements were carried out in Monolith capillaries (NanoTemper Technologies, MOK022) under the following instrument settings: 40% LED excitation power, medium MST power, and temperature maintained at 25 °C. Dissociation constants (Kd) were derived from 3 independent replicates using the NanoTemper MO.

Electrophoretic mobility shift assay

The electrophoretic mobility shift assay (EMSA) was performed using the LightShift Chemiluminescent EMSA Kit (20148, Thermo Scientific, MA, USA) following the manufacturer's instructions. Prior to the formal experiment, a probe concentration gradient screening was conducted with 5 gradients (0.01, 0.05, 0.1, 0.2, 0.5 μM), and 0.1 μM was ultimately selected as the optimal concentration to ensure specific binding with minimal nonspecific interference. Briefly, 45-bp oligonucleotide primers containing the cis-elements (Table S7) were synthesized, with biotin labeled at the 5′ end of both strands. The biotin-labeled probe at the optimal concentration (0.1 μM) was incubated with the target protein in the kit binding buffer at room temperature for 30 min. The reaction mixtures were separated on an 8% polyacrylamide gel in 0.5×TBE buffer, followed by membrane transfer and subsequent antibody incubation in accordance with the kit

Downloaded from academic.oup.com/plphys/article/202/2/kiag347/8704448 by Hangzhou Normal University user on 03 November 2026

protocol. For signal detection, gels for Fig. 4 and Fig. S8 were exposed to X-ray film for 48–96 h via film pressing, while that for Fig. S9 was visualized using a chemiluminescence imaging system (Thermo Fisher Scientific). Complementary pairs of biotin-labeled and unlabeled oligonucleotide probes are listed in Table S7. For the mutated probes, C to A and A to G transitions were done (Cerri et al. 2017). Preliminary results indicate that MtIPD3^{DD} (MtIPD3$^{50D,\ 155D}$) rather than MtIPD3, caused an electrophoresis mobility shift of probe covering the region of −2035 to −1503 (prob-α, clear), 1539 to −983 (prob-β, weak) or −1005 to −452 (prob-γ, faint), indicating potential protein-DNA interactions. Further analyses and fine mapping narrowed down the recognition motif to a stretch from −1931 to −1901. *TTTTGAAAACTTT* (*IPD3-RE$_{NIN}$*) carrying a nonpalindromic sequence, was deemed to be the target motif recognized by MtIPD3. To validate the recognition motif located at the very end of the EMSA probe, the 45 bp DNA from −1945 to −1901 carrying *IPD3-RE$_{NIN}$* (NIN-α2-1) was used for site-mutation based verification test. Our results showed that unlabeled probe contain wildtype *IPD3-RE$_{NIN}$* motif competed with biotin labeled probe for binding IPD3, while mutated probe with *IPD3-RE$_{NIN}$* mutated to *GGGGGGGGGGGGG* (α2-1-1m1) cannot compete with biotin labeled probe. This analysis demonstrated that cis-element *TTTTGAAAACTTT* (*IPD3-RE$_{NIN}$*) is required for MtIPD3^{DD} to bind the promoter of *MtNIN* gene.

Quantitative RT-PCR analyses

For evaluation of *MtNIN* transcriptional expression, *dmi3-1* roots transformed with *DMI3$^{WT\ or\ mutants}$* were collected 2 weeks post (wpi) rhizobia inoculation according to Jin et al (2016, 2018). As well, a time course (1, 2, 3 and 4 wpi) of *MtNIN* inductions were tested in *dmi3-1* roots transformed with *DMI3^{SST}*, *OsCCaMK^{SCK}*, and *OsCCaMK^{SST}* (Godfroy et al. 2006). Total RNA was extracted with the RNAiso Plus kit (Cat NO. 9109, TaKaRa, Kyoto, Japan). Approximately 2 μg of total RNA for each sample was reverse transcribed using a PrimeScript RT Master Mix (Cat NO. RR036A, TaKaRa). Real-time quantitative RT-PCR was performed in 10 μL reaction volume containing 1 μL of diluted (1:100) cDNA and 5 μL of 2X TB Green Fast qPCR Mix (Cat NO. RR430A, TakaRa) in a CFX96 real-time PCR system (BIORAD, Hercules, California, USA). The relative expression level was normalized against that of the Medicago *ubiquitin* (*Medtr4g091580*) gene (Feng et al. 2021). Three biological replicates were used for calculating the mean and standard error of each genotype. The primers used are shown in Table S8.

Mass spectrometry analysis

To prepare samples for MS analysis, 5 μg DMI3 were incubated in 40 μL kinase buffer containing 25 mM Tris-HCl (pH 7.6), 10 mM $MgCl_2$, 0.5 mM DTT and 1 mM ATP at 30 °C for 30 min. The reaction was stopped by SDS loading buffer and separated on 12% SDS-PAGE followed by Coomassie brilliant blue (CBB) staining. The desired band was excised and in-gel digestion with trypsin was performed as described previously (Pi et al. 2016). The peptides were analyzed using the Easy-nLC 1000-LTQ Obitrap ETD LC-MS/MS System (Thermo Scientific, MA, USA). The MS data were analyzed with Thermo Scientific Proteome Discoverer software (v.1.4), and the identified phosphorylated peptides list in Table S9. LC-MS/MS analysis was performed by the Micrometer Biotech Company (Hangzhou, China).

Calmodulin-binding assay

The Arabidopsis Calmodulin 2 protein was conjugated to maleimide activated horseradish peroxidase (AC2-HRP) according to the manufacturer's protocol (Cat NO. 31485, Thermo Scientific, MA, USA). Calmodulin-binding assays were performed as described previously (Routray et al. 2013) with minor modification. In brief, purified DMI3-His or its site-mutated proteins were separated by SDS-PAGE and transferred to a polyvinylidene difluoride membrane (Cat NO. IPFL00010, Merck Millipore, Darmstadt, Germany). The membrane was incubated with 10 μg AC2-HRP proteins in binding buffer containing 50 mM Tris-HCl (pH 7.4), 150 mM NaCl, 0.05% Tween 20, 1 mM $CaCl_2$, and 5% (w/v) skimmed milk powder at 4 °C for 2 h. The membrane was washed with TBST buffer (50 mM Tris-HCl, pH 7.4, 150 mM NaCl, 0.05% Tween 20) 3 times and visualized by CL-XPosure X-ray film (Cat NO. 34090, MA, USA).

Acetylene reductase assay

The acetylene reduction assay was conducted following David et al. (1980) with minor adjustments. Fresh root nodules were carefully washed with distilled water to eliminate soil debris, after which approximately 0.1 g of fresh tissue was precisely weighed and transferred into 100 mL glass bottles. Using a gas-tight syringe, 5 mL of the headspace atmosphere was removed and replaced with an equal volume of purified acetylene gas, resulting in a final concentration of ~5% (v/v) acetylene in the bottle. The bottles were incubated at 28 °C in complete darkness for 2 hours to facilitate nitrogenase-catalyzed acetylene conversion. Following incubation, a 500 μL gas sample was extracted and analyzed using an Agilent GC7890 gas chromatograph (Wilmington, USA). Ethylene production was quantified by measuring peak areas and converting the values to nmol μmol^{-1} C_2H_4 h^{-1} g^{-1} fresh weight (FW).

Prediction of target protein and complex structure models

The amino acid sequences of DMI3, IPD3, and CaM were downloaded from the Uniprot database in FASTA format. ExPASy ProtParam was used to analyze their physicochemical properties, including amino acid composition, molecular weight, isoelectric point (pI), hydrophobicity, instability index, and aliphatic index. SOPMA was applied to predict their secondary structures, calculating the proportions of α-helix, β-sheet, random coil, and extended strand, with emphasis on the calmodulin-binding domain (CBD, residues ~330 to 350) of DMI3 and the amino acid environment of S343, S344, and T345 sites.

AlphaFold 3 server was used for 3D structure prediction of protein monomers and complexes. For monomer structure prediction, the FASTA sequences of DMI3, IPD3, and CaM were separately uploaded to AlphaFold 3 in the default high-confidence mode, generating 5 candidate models for each protein, which were saved in PDB format. For complex structure prediction, 3 DMI3 mutants were constructed and comodeled with CaM and IPD3. Their FASTA sequences were couploaded to AlphaFold 3, with interaction regions set as CBD domain of DMI3 with CaM and kinase domain of DMI3 with IPD3.

Candidate models were initially screened based on pLDDT value (pLDDT ≥ 0.85 for core regions was optimal) and PAE value (lower values indicated higher structural reliability). The optimal model was manually optimized using PyMOL 2.5.3, including removing water molecules and heteroatoms, correcting distorted peptide bonds, and

Downloaded from academic.oup.com/plphys/article/202/2/kiag347/8704448 by Hangzhou Normal University user on 03 November 2026

complementing missing short amino acid residues. GROMACS software (AMBER99SB-ILDN force field) was used for energy minimization (10000 steps, convergence criterion: energy change ≤ 0.01 kJ/[mol·nm]).

PROCHECK, ERRAT, Verify3D, and PyMOL 2.5.3 were used for model quality verification. PROCHECK was used to analyze the Ramachandran plot, requiring ≥ 90% of residues in favored regions and ≤ 1% in disallowed regions. ERRAT was used to calculate the overall quality factor (≥ 80). Verify3D was used to analyze structure-sequence compatibility, requiring ≥ 80% of residues with 3D-1D score ≥ 0.2. Qualified models were saved in PDB format for subsequent experiments.

Molecular Docking

AutoDock Tools 1.5.6 was used for preprocessing of docking samples. For IPD3 (DNA-binding receptor) and DMI3 (CaM-binding receptor) and their mutants, water molecules and heteroatoms were removed, hydrogen atoms were added, protonation states were determined according to pH = 7.4, and Gasteiger charges were calculated. The active pockets were defined based on CASTp prediction and manuscript reports. For ligands (DNA motifs and CaM), 3D structures were constructed using Raschig 3D Structure Generator, optimized by energy minimization (MMFF94 force field, 5,000 steps, convergence criterion: energy change ≤ 0.05 kJ/(mol·nm)), and saved in PDBQT format.

AutoDock Vina 1.2.0 was used for molecular docking calculation. For IPD3-DNA docking, the grid size was set to 40 Å * 40 Å * 40 Å, with the center located near Arg-423 residue. For DMI3 (and its mutants)-CaM docking, the grid size was 35 Å * 35 Å * 35 Å, with the center located near T345 residue. The exhaustiveness was set to 16 for all docking experiments, and each combination was repeated 3 times to ensure reproducibility. Docking results were saved for subsequent analysis.

PyMOL 2.5.3 and UCSF Chimera 1.17 were used for docking result analysis. Binding energy was calculated as the average ± standard error (SE) of 3 replicates, with more negative values indicating stronger binding ability. PRODIGY server and MM/GBSA method were used to calculate binding affinity. The optimal binding conformation (lowest binding energy) was visualized to analyze binding posture, interface, and interaction types (hydrogen bonds, hydrophobic interactions, electrostatic interactions). The results were compared with EMSA and GST pull-down data in the manuscript to verify rationality.

Evolutionary analyses and logo plot for CaM-binding domain DMI3

Sequences of representative plant DMI3 proteins from 221 different species were retrieved from NCBI and their CaM-binding domain were aligned using MEGA7.0. The evolutionary history was inferred using the Minimum Evolution method and the evolutionary distances were computed using the Poisson correction method. The Neighbor-joining algorithm was used to generate the initial tree (Kumar et al. 2016).

An amino acid logo plot for the CaM-binding domain was created using Weblogo (http://weblogo.berkeley.edu/logo.cgi) as described previously (Chandler et al. 2018). The GenBank accession numbers are in Table S2.

Statistical analysis

All data were statistically analyzed using the program SPSS Statistics version 22.0 (IBM, Armonk, NY, USA). ANOVA corrected with Waller-Duncan k-ratio *t*-test was used to determine statistical significance ($P < 0.05$ as the level of significance).

Accession numbers

Sequence data from this article can be found in the GenBank/EMBL data libraries. All corresponding accession numbers are listed in Table S10.

Acknowledgments

The authors are grateful to Professor Ertao Wang at the Center for Excellence in Molecular Plant Sciences, Chinese Academy of Sciences, for kindly providing the rhizobia strain Sm2011-GFP. They also sincerely appreciate the reviewers for their valuable comments and constructive suggestions, which greatly improved the manuscript.

Author Contributions

E.P., S.W., and L.D. conceived the overall idea and designed the experiments, analyzed the data, and wrote the manuscript. E.P. and Y.Q. performed most of the experiments. X.L., Y.Z., Y.W., L.D., L.D., J.S., Q.G., K.J., and Y.H. performed Y2H, pull-down, RT-qPCR, EMSA, and RNS analysis.

Supplementary material

Supplementary material is available at *Plant Physiology* online.

Funding

This work was supported by grants from the National Science Foundation of China (grants No. 31970286 and U1130304), the Natural Science Foundation of Zhejiang Province (grants No. LY22C020001, LY17C020004 and LR20C020001), the Joint Funds of the Zhejiang Provincial Natural Science Foundation of China (grant No. LHZSZ24C010001), the Zhejiang Provincial Science and Technology Department (grant No. 2025SDXT004-2), the Hangzhou Joint Fund of Zhejiang Provincial Natural Science Foundation of China (Grant No. LHZQN25C130006), the Hangzhou Science and Technology Bureau (grants No. 20170432B01 and 20180432B11), and the State Key Laboratory of Subtropical Silviculture (grant No. SKLSS-KF2024-08).

Conflicts of interest

There is no conflict of interest.

Data availability

All data are available in the main text or the supplementary materials.

References

Abramson J *et al.* 2024. Accurate structure prediction of biomolecular interactions with AlphaFold 3. *Nature*. 630:493–500. https://doi.org/10.1038/s41586-024-07487-w.

Akamatsu A, Nagae M, Takeda N. 2022. The CYCLOPS response element in the NIN promoter is important but not essential for infection thread formation during *Lotus japonicus*-rhizobia symbiosis. *Mol Plant Microbe Interact*. 35:650–658. https://doi.org/10.1094/MPMI-10-21-0252-R.

Downloaded from academic.oup.com/plphys/article/202/2/kiag347/8704448 by Hangzhou Normal University user on 03 November 2026

Cao H *et al.* 2025. Ca2+-dependent cytoplasmic and nuclear phosphorylation of STOP1 by CPK21 and CPK23 confers ALMT1-dependent aluminum resistance. *Nat Commun*. 16:5225. https://doi.org/10.1038/s41467-025-60426-9.

Cathebras C *et al.* 2022. A novel *cis*-element enabled bacterial uptake by plant cells. *Nat Plants*. 2026;12:140–151. https://doi.org/10.1038/s41477-025-02161-z.

Catoira R *et al.* 2000. Four genes of *Medicago truncatula* controlling components of a nod factor transduction pathway. *Plant Cell*. 12:1647–1666. https://doi.org/10.1105/tpc.12.9.1647.

Cerri MR *et al.* 2017. The ERN1 transcription factor gene is a target of the CCaMK/CYCLOPS complex and controls rhizobial infection in *Lotus japonicus*. *New Phytol*. 215:323–337. https://doi.org/10.1111/nph.14547.

Cervera M. 2005. Histochemical and fluorometric assays for *uidA* (*GUS*) gene detection. *Methods Mol Biol*. 286:203–214. https://doi.org/10.1385/1-59259-827-7:203.

Chandler JW. 2018. Class VIIIb APETALA2 ethylene response factors in plant development. *Trends Plant Sci*. 23:151–162. https://doi.org/10.1016/j.tplants.2017.09.016.

David KAV, Apte SK, Banerji A, Thomas J. 1980. Acetylene reduction assay for nitrogenase activity: gas chromatographic determination of ethylene per sample in less than one minute. *Appl Environ Microb*. 39:1078–1080. https://doi.org/10.1128/aem.39.5.1078-1080.1980.

Ding ZJ *et al.* 2024. The LRR receptor-like kinase ALR1 is a plant aluminum ion sensor. *Cell Res*. 34:281–294. https://doi.org/10.1038/s41422-023-00915-y.

Du LQ *et al.* 2009. Ca^{2+}/calmodulin regulates salicylic-acid-mediated plant immunity. *Nature*. 457:1154–U1116. https://doi.org/10.1038/nature07612.

Ehrhardt DW, Wais R, Long SR. 1996. Calcium spiking in plant root hairs responding to Rhizobium nodulation signals. *Cell*. 85:673–681. https://doi.org/10.1016/S0092-8674(00)81234-9.

Feng J, Lee T, Schiessl K, Oldroyd GED. 2021. Processing of NODULE INCEPTION controls the transition to nitrogen fixation in root nodules. *Science*. 374:629–632. https://doi.org/10.1126/science.abg2804.

Gleason C *et al.* 2006. Nodulation independent of rhizobia induced by a calcium-activated kinase lacking autoinhibition. *Nature*. 441:1149–1152. https://doi.org/10.1038/nature04812.

Godfroy O, Debelle F, Timmers T, Rosenberg C. 2006. A rice calcium- and calmodulin-dependent protein kinase restores nodulation to a legume mutant. *Mol Plant Microbe In*. 19:495–501. https://doi.org/10.1094/MPMI-19-0495.

Gong X, Jensen E, Bucerius S, Parniske M. 2022. A CCaMK/Cyclops response element in the promoter of *Lotus japonicus Calcium-Binding Protein 1* (*CBP1*) mediates transcriptional activation in root symbioses. *New Phytol*. 235:1196–1211. https://doi.org/10.1111/nph.18112.

Hayashi T *et al.* 2010. A dominant function of CCaMK in intracellular accommodation of bacterial and fungal endosymbionts. *Plant J*. 63:141–154. https://doi.org/10.1111/j.1365-313X.2010.04228.x.

Herridge DF, Peoples MB, Boddey RM. 2008. Global inputs of biological nitrogen fixation in agricultural systems. *Plant Soil*. 311:1–18. https://doi.org/10.1007/s11104-008-9668-3.

Ito T, Ishida S, Oe S, Fukazawa J, Takahashi Y. 2017. Autophosphorylation affects substrate-binding affinity of tobacco ca-dependent protein Kinase1. *Plant Physiol*. 174:2457–2468. https://doi.org/10.1104/pp.17.00515.

Jarzyniak K *et al.* 2021. Early stages of legume-rhizobia symbiosis are controlled by ABCG-mediated transport of active cytokinins. *Nat Plants*. 7:428–436. https://doi.org/10.1038/s41477-021-00873-6.

Jauregui E, Du LQ, Gleason C, Poovaiah BW. 2017. Autophosphorylation of calcium/calmodulin-dependent protein kinase (CCaMK) at S343 or S344 generates an intramolecular interaction blocking the CaM-binding. *Plant Signal Behav*. 12:e1343779. https://doi.org/10.1080/15592324.2017.1343779.

Jin Y *et al.* 2016. DELLA proteins are common components of symbiotic rhizobial and mycorrhizal signalling pathways. *Nat Commun*. 7: ARTN 12433. https://doi.org/10.1038/ncomms12433.

Jin Y *et al.* 2018. IPD3 and IPD3L function redundantly in rhizobial and mycorrhizal symbioses. *Front Plant Sci*. 9:ARTN 267. https://doi.org/10.3389/fpls.2018.00267.

Kang H *et al.* 2011. A novel interaction between CCaMK and a protein containing the scythe_N ubiquitin-like domain in *Lotus japonicus*. *Plant Physiol*. 155:1312–1324. https://doi.org/10.1104/pp.110.167965.

Kim DS, Hwang BK. 2011. The pepper receptor-like cytoplasmic protein kinase CaPIK1 is involved in plant signaling of defense and cell-death responses. *Plant J*. 66:642–655. https://doi.org/10.1111/j.1365-313X.2011.04525.x.

Kumar S, Stecher G, Tamura K. 2016. MEGA7: molecular evolutionary genetics analysis version 7.0 for bigger datasets. *Mol Biol Evol*. 33:1870–1874. https://doi.org/10.1093/molbev/msw054.

Lerouge P *et al.* 1990. Symbiotic host-specificity of *Rhizobium meliloti* is determined by a sulphated and acylated glucosamine oligosaccharide signal. *Nature*. 344:781–784. https://doi.org/10.1038/344781a0.

Lévy J *et al.* 2004. A putative Ca^{2+} and calmodulin-dependent protein kinase required for bacterial and fungal symbioses. *Science*. 303:1361–1364. https://doi.org/10.1126/science.1093038.

Liao JQ *et al.* 2012. Negative regulation of CCaMK is essential for symbiotic infection. *Plant J*. 72:572–584. https://doi.org/10.1111/j.1365-313X.2012.05098.x.

Limpens E, Bisseling T. 2014. CYCLOPS: a new vision on rhizobium-induced nodule organogenesis. *Cell Host Microbe*. 15:127–129. https://doi.org/10.1016/j.chom.2014.01.015.

Lindsay PL, Williams BN, MacLean A, Harrison MJ. 2019. A phosphate-dependent requirement for transcription factors IPD3 and IPD3L during arbuscular mycorrhizal symbiosis in *Medicago truncatula*. *Mol Plant Microbe In*. 32:1277–1290. https://doi.org/10.1094/MPMI-01-19-0006-R.

Liu JY *et al.* 2019. A remote *cis*-regulatory region is required for expression in the pericycle to initiate nodule primordium formation in *Medicago truncatula*. *Plant Cell*. 31:68–83. https://doi.org/10.1105/tpc.18.00478.

Liu L *et al.* 2021. BRASSINOSTEROID-SIGNALING KINASE 1 phosphorylating CALCIUM/CALMODULIN-DEPENDENT PROTEIN KINASE functions in drought tolerance in maize. *New Phytol*. 231:695–712. https://doi.org/10.1111/nph.17403.

Malkov N *et al.* 2016. Molecular basis of lipo-chitooligosaccharide recognition by the lysin motif receptor-like kinase LYR3 in legumes. *Biochem J*. 473:1369–1378. https://doi.org/10.1042/BCJ20160073.

Marsh JF *et al.* 2007. *Medicago truncatula* NIN is essential for rhizobial-independent nodule organogenesis induced by autoactive calcium/calmodulin-dependent protein kinase. *Plant Physiol*. 144:324–335. https://doi.org/10.1104/pp.106.093021.

Messinese E *et al.* 2007. A novel nuclear protein interacts with the symbiotic DMI3 calcium- and calmodulin-dependent protein kinase of *Medicago truncatula*. *Mol Plant Microbe Interact*. 20:912–921. https://doi.org/10.1094/MPMI-20-8-0912.

Miller JB *et al.* 2013. Calcium/calmodulin-dependent protein kinase is negatively and positively regulated by calcium, providing a mechanism for decoding calcium responses during symbiosis signaling. *Plant Cell*. 25:5053–5066. https://doi.org/10.1105/tpc.113.116921.

Mitra RM *et al.* 2004. A Ca^{2+}/calmodulin-dependent protein kinase required for symbiotic nodule development: gene identification by transcript-

Downloaded from academic.oup.com/plphys/article/202/2/kiag347/8704448 by Hangzhou Normal University user on 03 November 2026

based cloning. *P Natl Acad Sci USA*. 101:4701–4705. https://doi.org/10.1073/pnas.0400595101.

Ouyang SQ *et al.* 2010. Receptor-like kinase OsSIK1 improves drought and salt stress tolerance in rice (*Oryza sativa*) plants. *Plant J*. 62:316–329. https://doi.org/10.1111/j.1365-313X.2010.04146.x.

Patil S, Takezawa D, Poovaiah BW. 1995. Chimeric plant calcium/calmodulin-dependent protein-kinase gene with a neural visinin-like calcium-binding domain. *Proc Natl Acad Sci U S A*. 92:4897–4901. https://doi.org/10.1073/pnas.92.11.4897.

Pi EX *et al.* 2016. Mechanisms of soybean roots' tolerances to salinity revealed by proteomic and phosphoproteomic comparisons between two cultivars. *Mol Cell Proteomics*. 15:266–288. https://doi.org/10.1074/mcp.M115.051961.

Pimprikar P *et al.* 2016. A CCaMK-CYCLOPS-DELLA complex activates transcription of RAM1 to regulate arbuscule branching. *Curr Biol*. 26:1126–1126. https://doi.org/10.1016/j.cub.2016.04.021.

Routray P, Miller JB, Du LQ, Oldroyd G, Poovaiah BW. 2013. Phosphorylation of S344 in the calmodulin-binding domain negatively affects CCaMK function during bacterial and fungal symbioses. *Plant J*. 76:287–296. https://doi.org/10.1111/tpj.12288.

Sathyanarayanan PV, Siems WF, Jones JP, Poovaiah BW. 2001. Calcium-stimulated autophosphorylation site of plant chimeric calcium/calmodulin-dependent protein kinase. *J Biol Chem*. 276:32940–32947. https://doi.org/10.1074/jbc.M009648200.

Schauser L, Roussis A, Stiller J, Stougaard J. 1999. A plant regulator controlling development of symbiotic root nodules. *Nature*. 402:191–195. https://doi.org/10.1038/46058.

Schulte CCM *et al.* 2021. Metabolic control of nitrogen fixation in rhizobium-legume symbioses. *Sci Adv*. 7:eabh2433. https://doi.org/10.1126/sciadv.abh2433.

Shen DF *et al.* 2020. A homeotic mutation changes legume nodule ontogeny into actinorhizal-type ontogeny. *Plant Cell*. 32:1868–1885. https://doi.org/10.1105/tpc.19.00739.

Shimoda Y *et al.* 2012. Rhizobial and fungal symbioses show different requirements for calmodulin binding to calcium calmodulin-dependent protein kinase in *Lotus japonicus*. *Plant Cell*. 24:304–321. https://doi.org/10.1105/tpc.111.092197.

Singh S, Katzer K, Lambert J, Cerri M, Parniske M. 2014. CYCLOPS, a DNA-binding transcriptional activator, orchestrates symbiotic root nodule development. *Cell Host Microbe*. 15:139–152. https://doi.org/10.1016/j.chom.2014.01.011.

Takeda N, Maekawa T, Hayashi M. 2012. Nuclear-localized and deregulated calcium- and calmodulin-dependent protein kinase activates rhizobial and mycorrhizal responses in Lotus japonicus. *Plant Cell*. 24:810–822. https://doi.org/10.1105/tpc.111.091827.

Takezawa D, Ramachandiran S, Paranjape V, Poovaiah BW. 1996. Dual regulation of a chimeric plant serine/threonine kinase by calcium/calmodulin. *J Biol Chem*. 111:155–155. https://doi.org/10.1074/jbc.271.14.8126.

Tirichine L *et al.* 2006. Deregulation of a Ca^{2+}/calmodulin-dependent kinase leads to spontaneous nodule development. *Nature*. 441:1153–1156. https://doi.org/10.1038/nature04862.

Wang DP, Dong WT, Murray J, Wang ET. 2022. Innovation and appropriation in mycorrhizal and rhizobial symbioses. *Plant Cell*. 34:1573–1599. https://doi.org/10.1093/plcell/koac039.

Yano K *et al.* 2008. CYCLOPS, a mediator of symbiotic intracellular accommodation. *Proc Natl Acad Sci U S A*. 105:20540–20545. https://doi.org/10.1073/pnas.0806858105.

Zheng KJ *et al.* 2024. The proteome of *Nicotiana benthamiana* is shaped by extensive protein processing. *New Phytol*. 243:1034–1049. https://doi.org/10.1111/nph.19891.

Downloaded from academic.oup.com/plphys/article/202/2/kiag347/8704448 by Hangzhou Normal University user on 03 November 2026